Clouds and the Earth's Radiant Energy System (CERES)

Algorithm Theoretical Basis Document

Imager Clear-Sky Determination and Cloud Detection

(Subsystem 4.1)

CERES Science Team Cloud Retrieval Working Group

Bryan A. Baum[1]
Ronald M. Welch[2]
Pat Minnis[1]
Larry L. Stowe[3]
James A. Coakley, Jr. [4]

Algorithm Implementation, Data Analysis, and Data Management

Qing Trepte[5]
Pat Heck[6]
Xiquan Dong[6]
Dave Doelling[6]
Sunny Sun-Mack[5]
Tim Murray[5]

Automated Classification Techniques and Algorithm Development

Todd Berendes[2]
Kwo-Sen Kuo[2]
Paul Davis[3]

[1]Atmospheric Sciences Division, NASA Langley Research Center, Hampton, Virginia 23681-0001

[2]South Dakota School of Mines and Technology, Rapid City, South Dakota 57701-3995

[3]Satellite Research Laboratory, National Oceanic and Atmospheric Administration, 5200 Auth Road, Camp Springs, Maryland 20746

[4]Department of Atmospheric Sciences, Oregon State University, Corvallis, Oregon 97331-2209

[5]Science Applications International Corporation (SAIC), Hampton, Virginia 23666

[6]Analytical Services & Materials, Inc., Hampton, Virginia 23666

June 2, 1997

CERES Top Level D

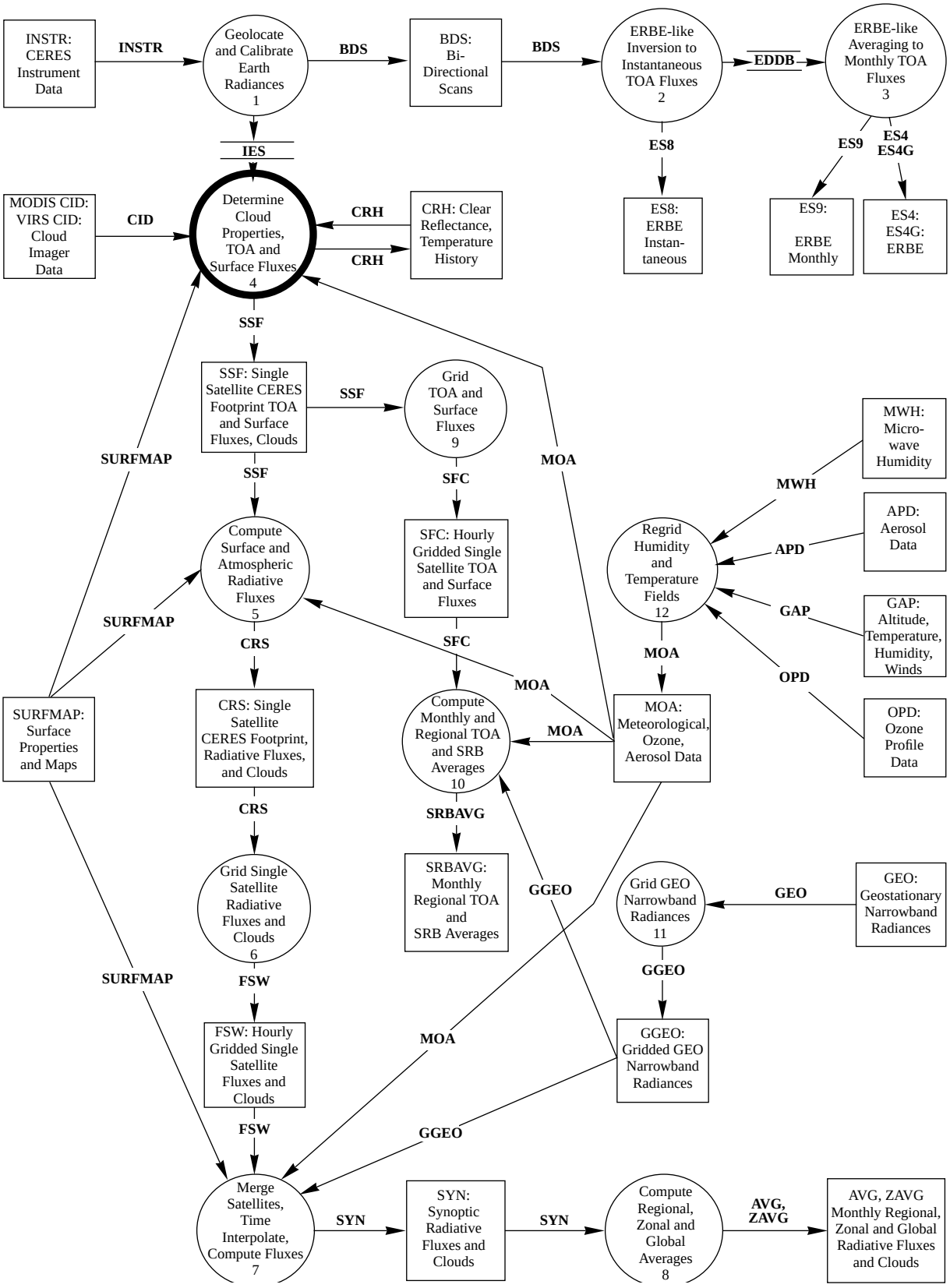

4.1. Imager Clear-Sky Determination and Cloud Detection

4.1.1. Overview

This document outlines the methodology for the CERES Release 2 global cloud mask and subsequent generation of global clear-sky temperature and albedo maps. The cloud mask will be applied to the appropriate imager data stream for TRMM or EOS (VIRS or MODIS, respectively). Originally, the purpose of this software was to determine those pixels that contained cloud; all other pixels were deemed as containing clear-sky conditions. Recently, however, we have received continuing feedback from one of the primary users of this product - the Surface and Atmsopheric Radiation Budget (SARB) group (CERES Subsystem 5). Their feedback has led to significant modifications to the requirements of cloud/clear-sky detection effort. The SARB group has requested that we identify what a pixel contains if it does not have cloud. More precisely, the goal of this effort has changed to determine if noncloudy imager pixels contain smoke, fire, sunglint, surface snow, or sea ice. The output from this algorithm is a pixel-level mask that includes information about whether the pixel contains cloud, clear-sky, snow/sea ice, smoke, fire, or sunglint.

The cloud mask is being designed currently for the narrowband channels on both the AVHRR and VIRS instruments. The additional capabilities afforded by the MODIS instrument will be addressed in Release 3 of this document. The members of the CERES and MODIS cloud mask development teams are working closely together to develop a coordinated cloud mask approach. We anticipate that the eventual MODIS cloud mask algorithm will be incorporated and modified for use by CERES. Further discussion on the MODIS/CERES cloud mask issue is provided in Section 4.1.1.2.

The CERES approach as envisioned in Release 2 is provided in more detail in Section 4.1.1.2. Part of the CERES cloud masking algorithm relies heavily upon a rich heritage of both NASA and NOAA experience with global data analysis. Our algorithm design has incorporated many aspects of the approaches used by ISCCP (International Satellite Cloud Climatology Project) (Rossow and Garder 1993), CLAVR (Clouds from AVHRR) (Stowe et al. 1991), and SERCAA (Support of Environmental Requirements for Cloud Analysis and Archive). The ISCCP algorithms are based upon two channels, one in the visible wavelength region and one in the infrared. The CLAVR approach uses all five channels of the AVHRR instrument. The CLAVR multispectral threshold approach uses narrowband channel differences, ratio tests, single channel threshold tests, and includes dynamic threshold specification with clear-sky radiation statistics. The SERCAA algorithm is operational at the Phillips Laboratory, Hanscom Air Force Base, and uses all five AVHRR radiometric channels. The SERCAA is sponsored jointly by the Department of Defense, Department of Energy, and Environmental Protection Agency Strategic Environmental Research and Development Program. The major departure from these operational masking schemes, and a major change from Version 1 of this document, is the use of new modules designed for analysis in complex instances when the application of individual sequential threshold tests is insufficient. Several examples of complex situations include discerning clouds from snow or sea ice, clouds in sunglint regions, distinguishing smoke from clouds in biomass burning areas, and distiguishing between blowing dust and clouds in desert regions.

Section 4.1.2 discusses the input imager and ancillary data and assumptions made about the data, the preprocessing process and the output data. The classical threshold test approach is outlined in Section 4.1.3.2, and the new cloud masking modules for complex situations is described in Sectin 4.1.3.3. The clear-sky map scheme is outlined in Section 4.1.4, and cloud contamination tests using the clear-sky maps are presented in Section 4.1.5. A brief discussion on future efforts is presented in Section 4.1.6.

4.1.1.2. The CERES Approach

In Version 1, CERES combined a series of threshold tests based on SERCAA, ISCCP, and CLAVR. As a result of Version 1 testing, a simplified scheme was developed and implemented for Version 2. A flow chart for the suite of threshold tests is shown in Figure 4.1-1 for daytime and nighttime analyses. A detailed description of each threshold test is provided in Section 4.1.3. Our experience with this set of threshold tests has been that most of the clouds are masked immediately using either a reflectance threshold (based on AVHRR channel 1 or 2) or a thermal channel threshold (based on AVHRR channels 4 or 5). The problems occur primarily for the following situations:

a. very thin cloud (e.g., cirrus, cloud edges)

b. sunglint regions

c. surfaces covered with snow or ice

d. areas of extensive biomass burning containing fires and/or smoke

e. nonvegetated surfaces with nonuniform emissivity, such as deserts

f. nighttime analyses involving low-level cloud with near-surface temperatures

g. surface conditions varying rapidly, e.g., due to frontal conditions

Further, the Surface and Atmospheric Radiation Budget (SARB) group has stated that in addition to specifying whether a pixel contains cloud, it would be very beneficial if other information could be ascertained, such as whether there was sunglint, smoke, fires, or surface snow/sea-ice. To attain these goals, we have developed a set of modules that are described in detail in Section 4.1.3.3.

The snow/ice module (Section 4.1.3.3.3) has been tested extensively with daytime AVHRR data with good results. The same suite of tests have been tested independently by the MODIS cloud mask team at the Space Science Engineering Center at the University of Wisconsin-Madison. The tests are also being tested by the SERCAA group at the Air Force Geophysics Lab in Boston and also the MODIS snow group at NASA Goddard Space Flight Center.

Cloud discrimination over mountainous regions is an area of active research. It is just becoming known to our group that the Data Assimilation Office (DAO) gridded meteorological products are typically cold in mountainous regions (at least for GEOS-1). The use of DAO data in the cloud detection algorithm is discussed further in Section 4.1.4.

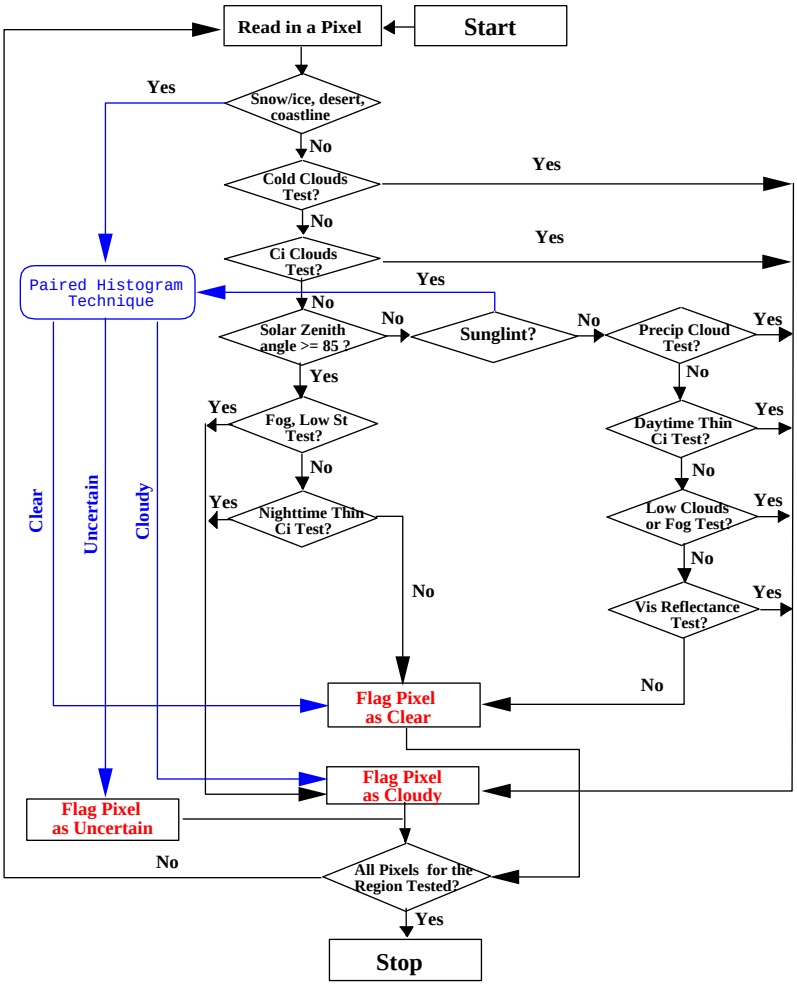

Figure 4.1-1. Schematic of CERES Version 2 cloud mask algorithm. Note that in addition to the application of sequential threshold tests as in Version 1, there are now modules that have developed specifically to address problem areas such as clouds in sunglint areas, clouds over snow/sea ice, clouds in regions containing biomass burning, and clouds over deserts.

Some of the stated problems can not be resolved using AVHRR or VIRS data, but can be addressed once MODIS data become available. For instance, the 1.38-μm channel will detect thin cirrus (Gao et al. 1993). Since 1994, there has been a collaboration between CERES and MODIS personnel in developing a cloud mask for MODIS. We anticipate that the ultimate algorithm developed as part of this effort will be used by CERES at the time of the EOS-AM launch. The question has been asked: What

are the practical implications of CERES importing the MODIS cloud mask product instead of processing the MODIS data stream at the Langley DAAC?

There are several aspects of this question that we can address.

1. A major thrust of the CERES effort is to develop a new set of Angular Distribution Models (ADM's). For this effort to take place, the data stream must be processed for approximately two years with no change in algorithms. If CERES were to import the MODIS cloud mask product instead of processing the MODIS data stream at the Langley DAAC, there would have to be an agreement with MODIS to provide the mask with no change in algorithm for the time period required to develop ADM's. Additionally, the MODIS team would have to agree to return values for the presence of sunglint, snow/sea ice, fire, smoke, etc. that the SARB group requires in their processing.

2. The MODIS cloud mask product, Version 2, is anticipated to contain 6 bytes of mask information per 1-km pixel, plus metadata and geolocation data. At the time of this writing, the current estimate of MODIS cloud mask product is approximately 40 bytes/pixel. Per day, this works out to about 31 GB. The reason for carrying so much metadata is to provide an end user with information about each test performed, the "quality" of the mask, and also information about sixteen collocated 0.25-km visible-channel pixels. Some of the metadata is unnecessary for CERES purposes. Given the complexity of obtaining another ancillary data file (in this case, the MODIS cloud mask product) and the large product volume, we think it would be much simpler to process the Level 1-B data stream at the Langley DAAC.

3. The same MODIS channels required for the masking process are required by CERES anyway to derive cloud properties. There would be no savings in MODIS Level 1-B data transfer.

4. As shown by the timing tests being performed by the CERES cloud working group (CERES Subsystem 4.0), the processing load for the cloud mask effort is anticipated to be near real-time.

Given these considerations, it seems more practical to use the initial MODIS cloud mask algorithm, modify it for use in the CERES production code (by "modify" we mean the process of getting the algorithm to work in the CERES production system, not tinkering with the algorithms), and process the MODIS data stream at the Langley DAAC. In the future, when CERES is ready to reprocess the MODIS data stream from the beginning, we will incorporate the most recent version of the MODIS cloud mask algorithm.

4.1.2. Data

4.1.2.1. Assumptions

Anyone who has worked with data measured in the field quickly comes to realize that the real world is less than perfect. A number of assumptions may be listed that attempt to place boundaries on the cloud mask task.

1. Satellite data used as input to the cloud mask algorithm is calibrated.
2. Satellite level 1-B data, for some imaging instruments, may be striped (like the GOES scanner) or have some "smearing" at high viewing scan angles. We assume that the data contains no striping or smearing.
3. The mask will be provided for "good" data only, i.e., for those narrowband channels that have radiometric integrity. For instance, the AVHRR 3.7-μm channel is sometimes too noisy to permit

accurate analysis of the radiometric data. This assumption implies that there may be holes in the mask if the data are incomplete.

4. The system level integration issues associated with implementation of this algorithm will not be raised in this subsystem document.
5. Sea surface temperature, surface snow/ice coverage, and operational National Meteorological Center gridded analysis products are assumed to be available for the operational cloud mask algorithm.
6. Smoke from forest fires, dust storms over deserts, and other surface phenomena that result in obstructing the field of view between the surface and the satellite may be considered as “cloud”.

4.1.2.1.1. Input data. The primary input data sets for subsystem 4.1 are the AVHRR GAC (global area coverage) satellite data and the following ancillary data sets:

- 1-min resolution coastline map, with lakes, rivers, islands, state/country boundaries
- 10-min resolution Navy digital elevation map
- 10-min resolution Internation Geosphere Biosphere Programme (IGBP) ecosystem map
- 60-km resolution daily NOAA Snow Data Product
- NCEP or DAO gridded meteorological analysis product
- 10-min resolution Navy character map (Table 4.1-1). Note that the character map provides a more general surface classification than the EPA ecosystem map.

Table 4.1-1.

Code	Feature
0	Salt or lake bed
1	Flat or relatively flat
2	Desert (or for high latitudes, glaciers, or permanent ice)
3	Marsh
4	Lake country or atoll
5	Major valleys or river beds
6	Isolated mountains, ridge, or peak
7	Low mountains
8	Mountainous
9	Extremely rugged mountains
62	Ocean

The CERES team is aware of the higher resolution ecosystem, land/water, and digital elevation maps becoming available. For the current problem of developing global algorithms using 4-km AVHRR Global Area Coverage data, the use of the 10-minute maps is deemed sufficient.

The spatial resolution of the AVHRR GAC data is about 4 km at nadir. The spectral data include AVHRR channels 1 (0.55–0.68 μm), 2 (0.725–1.1 μm), 3 (3.55–3.93 μm), 4 (10.5–11.5 μm), and 5 (11.5–12.5 μm), which include visible, near-infrared, and infrared window regions. The NOAA-11 central wave numbers for the AVHRR IR channels are (see Kidwell 1991).

Table II.

Temperature Range (K)	Ch 3 (cm^{-1})	Ch 4 (cm^{-1})	Ch 5 (cm^{-1})
180-225	2663.50	926.80	837.75
225-275	2668.15	927.34	838.08

Table II.

275-320	2671.40	927.80	838.40
270-310	2670.95	927.73	838.35

The values shown in Table 4.1-2 are slightly different for other sensors in this series of instruments. The VIRS instrument has a 720-km swath width with spectral measurements at channels 1 (0.63± 0.05 μm), 2 (1.60 ±0.03 μm), 3 (3.75±0.19 μm), 4 (10.8±0.5 μm), and 5 (12.0±0.5 μm). The channel 1 pixel brightness values were converted to radiances using calibration results reported by Rao et al. (1994). Channel 2 brightness values were converted to radiances using similar calibration results (Whitlock, personal communication 1994). The VIS radiances were converted to bidirectional reflectances ρ_i by

$$\rho_i = \frac{\pi I_i}{\mu_o F_i} \quad , \tag{4.1-1}$$

where *i* refers to channel 1 or 2, I_i is the shortwave spectral radiance in AVHRR channel *i*, F_i is the incoming solar spectral flux for channel *i*, and m_o is the cosine of the solar zenith angle. The NIR and IR radiances are calculated from the raw counts provided in the NOAA Level 1-B data stream using the nominal calibration (Kidwell 1991). AVHRR IR channel brightness temperatures include nonlinearity corrections reported by Weinreb et al. (1990).

The daytime 3.7-μm measured radiance contains contributions from both solar reflection and thermal emission. For masking purposes, the AVHRR 3.7-μm radiometric data (channel 3) are converted to reflectance through the relationship derived by Allen et al. (1990):

$$\rho_3 = \frac{I_3 - B_3\left(T_{B4}\right)}{F_3 \cos\theta_0 - B_3\left(T_{B4}\right)} \quad , \tag{4.1-2}$$

where I_3 and F_3 are the measured radiance and incoming solar flux for channel 3, respectively, and θ_0 is the solar zenith angle. The 3.7-μm thermal emission is estimated by using the 10.8-μm brightness temperature (T_{B4}) to solve the Planck function, $B_3(T_{B4})$. The reflectance calculated in this fashion is considered as an AVHRR "pseudochannel" and is used extensively in discriminating between clouds and snow, sea ice, smoke, and sunglint. Further details on these masking issues will be forthcoming.

4.1.2.1.2. Preprocessing of Imager Data

A number of preprocessing steps are performed on the imager data before the cloud masking algorithm is applied. The imager data processing scheme is outlined in Subsystem 4.0. Each imager pixel in the scene is labeled with the following characteristics before the cloud masking process begins: ecosystem, potential for sun glint, land/water percentage (note that this comes from a 10-minute database; in the future, a higher resolution surface map will be incorporated), surface snow or ice, and elevation. Additionally, the CERES team is gaining experience in how to generate and incorporate clear-sky radiance maps in the cloud masking process.

4.1.2.1.2. Output data. The output from the cloud mask algorithm is an integer that identifies whether the pixel contains: cloud, clear sky, smoke, fire, snow/sea ice, sunglint, or shadow. A cloud mask is derived for each imager pixel. The mask will be derived for the highest spatial resolution data

available. The final decision as to whether the pixel is obstructed or not is based upon the various cloud mask tests applied during the course of the algorithm. The final decision is stored in the appropriate slot in Table 4.4-1 for smoke, fire, snow/sea ice, sunglint, or shadow. For the VIRS instrument, the cloud fraction will be either a "0" or a "1." For validation purposes only, a separate output data structure will be implemented that stores the results from the individual tests.

4.1.3. Cloud Masking Threshold Algorithms

4.1.3.1. Heritage Approaches

Clouds generally are characterized by higher albedos and lower temperatures than the underlying surface. However, there are numerous conditions when this characterization is inappropriate, most notably over snow and ice. Of the cloud types, cirrus, low stratus, and small cumulus are the most difficult to detect. Likewise, cloud edges are difficult to recognize when they do not completely fill the field of view (FOV) of the imager pixel. The cloud mask effort builds upon operational experience of several groups that will now be discussed.

The NOAA CLAVR algorithm (Phase I) uses all five channels of AVHRR to derive a global cloud mask (Stowe et al. 1991). It examines multispectral information, channel differences, and spatial differences and then employs a series of sequential decision tree tests. Cloud-free, mixed (variable cloudy), and cloudy regions are identified for 2×2 GAC pixel arrays. If all four pixels in the array fail all the cloud tests, then the array is labeled as cloud-free (0% cloudy); if all four pixels satisfy just one of the cloud tests, then the array is labeled as 100% cloudy. If one to three pixels satisfy a cloud test, then the array is labeled as mixed and assigned an arbitrary value of 50% cloudy. If all four pixels of a mixed or cloudy array satisfy a clear-restoral test (required for snow/ice, ocean specular reflection, and bright desert surfaces) then the pixel array is reclassified as "restored-clear" (0% cloudy). The set of cloud tests is subdivided into daytime ocean scenes, daytime land scenes, nighttime ocean scenes, and nighttime land scenes.

Subsequent phases of CLAVR, now under development, will use dynamic clear/cloud thresholds predicted from the angular pattern observed from the clear sky radiance statistics of the previous 9-day repeat cycle of the NOAA satellite for a mapped 1° equal area grid cell (Stowe et al. 1994). As a further modification, CLAVR will include pixel by pixel classification based upon different threshold tests to separate clear from cloud contaminated pixels, and to separate cloud contaminated pixels into partial and total (overcast) cover. Cloud contaminated pixels will be radiatively "typed" as belonging to low stratus, thin cirrus, and deep convective cloud systems. A fourth type is middle mixed which includes all other cloud types.

The International Satellite Cloud Climatology Project (ISCCP) cloud masking algorithm is described by Rossow (1989), Rossow and Gardner (1993), and Seze and Rossow (1991a, b). Only two channels are used, the narrowband VIS (0.6 μm) and the IR (11 μm). Each observed radiance value is compared against its corresponding Clear-Sky Composite value. This step uses VIS radiances, not VIS reflectances. Clouds are assumed to be detected only when they alter the radiances by more than the uncertainty in the clear values. In this way the "threshold" for cloud detection is the magnitude of the uncertainty in the clear radiance estimates. As such this algorithm is not a constant threshold method such as used in Phase I of the CLAVR algorithm.

The ISCCP algorithm is based on the premise that the observed VIS and IR radiances are caused by only two types of conditions, "cloudy" and "clear," and that the ranges of radiances and their variability that are associated with these two conditions do not overlap (Rossow and Garder 1993). As a result, the algorithm is based upon thresholds, where a pixel is classified as "cloudy" only if at least one radiance value is distinct from the inferred "clear" value by an amount larger than the uncertainty in that "clear" value. The uncertainty can be caused both by measurement errors and by natural variability. This algo-

rithm is constructed to be “cloud-conservative,” minimizing false cloud detections but missing clouds that resemble clear conditions.

The ISCCP cloud-detection algorithm consists of five steps (Rossow and Garder 1993):

1. Space contrast test on a single IR image
2. Time contrast test on three consecutive IR images at constant diurnal phase
3. Cumulation of space/time statistics for IR and VIS images
4. Construction of clear-sky composites for IR and VIS every 5 days at each diurnal phase and location
5. Radiance threshold for IR and VIS for each pixel

Parts of the ISCCP scheme will be incorporated into the CERES cloud mask. Some modifications are necessary since all the AVHRR channels will be used, not just the visible and infrared channels (AVHRR channels 1 and 4).

The Support of Environmental Requirements for Cloud Analysis and Archive (SERCAA) algorithm from the Air Force uses multispectral AVHRR data to derive a global cloud mask. The SERCAA cloud decision tree consists of a series of cloud tests and background filter tests to identify cloudy and clear scenes using multispectral data and empirical thresholds. The algorithm is performed on a pixel-by-pixel basis. Percent albedo of channel 1 and channel 2 used in SERCAA has been changed to reflectance for CERES analysis.

4.1.3.2 Basic Cloud Detection Threshold Tests

In Version 1, imager data were processed for either cloud or clear using sets of sequential threshold tests defined later in this section. Note the exceptions to this general scheme, such as for regions that contain snow, ice, sunglint, smoke, and fires. While the CERES cloud masking effort initially was set up to perform cloud versus clear determinations, it soon became apparent through interaction with the Surface and Atmospheric Radiation Budget (SARB) group that more information about the surface was required, such as whether smoke was present, or snow, or ice. As the requirements changed, our approach to cloud masking has changed accordingly.

Generalized threshold tests are used for analysis of nighttime data and daytime data over certain regions such as oceans away from sunglint. For nighttime analysis, only the NIR and IR channels are available for cloud masking, and it is problematic to distinguish between clouds and snow-covered surfaces, clouds and smoke, etc. For daytime analysis, we have been able to make progress in discriminating between clouds and smoke over forested surfaces, but not yet surfaces designated as cropland, grassland, or savannah (i.e. non-forested land).

A detailed description of each basic cloud detection threshold test follows.

4.1.3.2.1 IR Threshold Tests (for both daytime and nighttime)

4.1.3.2.1.1 Cold Cloud Test

The Cold Cloud Test uses a single IR channel to discriminate the thermal signature of midlevel clouds from the terrestrial background. A cloud decision is made by comparing the channel 4 brightness temperature T_{B4}, with the clear scene brightness temperature T_{cs}. When T_{B4} is lower than T_{cs} by a amount greater than a preset threshold, the pixel is classified as cloudy. The test is defined as:

$$T_{cs} - T_{B4} > \text{Threshold}_{\text{cold}} \tag{4.1-3}$$

where Threshold_{cold} is the surface-dependent threshold shown in the following table:

Table 4.1-3.

Surface background	Threshold (K)
Water	9.0
Land	10.0

Current work being performed for Release 2 will further investigate the thresholds required for a range of surface types, including the various deserts, mountains, and other difficult ecosystem/ terrain types. In Release 1, a set of thresholds was provided for deserts, coastlines, and snow-covered surfaces. In Release 2, a new approach is implemented for complex areas and is discussed further in section 4.1.3.3.

4.1.3.2.1.2. Cirrus Cloud Tests

The brightness temperature difference between channel 4 and channel 5 ($T_{B4} - T_{B5}$, or BTD[45]) exhibits a persistent cirrus cloud signature based on the fact that cirrus cloud brightness temperatures are consistently higher at 10.7 μm than at 11.8 μm. However, in the absence of cloud, water vapor attenuation can cause a positive BTD[45] that could be mistaken for a cloud signature. Thus, the cloud detection threshold is defined as a function of the channel 4 brightness temperature T_{B4} and viewing zenith angle θ (to account for atmospheric path length). Table 4.1-4 contains the threshold values for a range of T_{B4} and θ developed by Saunders and Kriebel (1988) used as the basis in the Cirrus Cloud Test.

Table 4.1-4.

	Threshold for sec(θ) of—				
T_{B4}	1.00	1.25	1.50	1.75	2.00
260	0.55	0.60	0.65	0.90	1.10
270	0.58	0.63	0.81	1.03	1.13
280	1.30	1.61	1.88	2.14	2.30
290	3.06	3.72	3.95	4.27	4.73
300	5.77	6.92	7.00	7.42	8.43
310	9.41	10.74	11.03	11.60	13.39

The cirrus cloud test is defined as

$$T_{B4} - T_{B5} > \text{Threshold}\,(T_{B4}, \theta) \tag{4.1-4}$$

It can apply to both daytime and nighttime.

4.1.3.2.2. Daytime Threshold Tests

4.1.3.2.2.1 Thin Cirrus Cloud Test

The Daytime SERCAA Thin Cirrus Cloud Test utilizes the results from the solar independent Cirrus Cloud Test and the reflectance of channel 1 and channel 2. Recall the Cirrus Cloud Test requires the following conditions to be met:

$$T_{B4} - T_{B5} > \text{Threshold}\,(T_{B4}, \theta) \tag{4.1-5}$$

where Threshold (T_{B4}, θ) is the cloud detection threshold obtained through interpolation from Table 4.1-4.

If the background is classified as snow or ice covered, the module described in Section 4.1.3.3.3 is employed.

In addition to the tests listed above, the Daytime Thin Cirrus Cloud Test uses reflectance of channel 1 (ρ_1) to discriminate thin cirrus. The criterion used is dependent on the background surface type:

$$\rho_1 < \text{Threshold}_{dci\_w} \quad \text{(Over water)} \tag{4.1-6}$$

$$\rho_1 < \text{Threshold}_{dci\_l} \quad \text{(Over land)} \tag{4.1-7}$$

where Threshold_{dci_w} and Threshold_{dci_l} are the cloud detection threshold values over water and land, respectively, $\text{Threshold}_{dci\_w} = 0.2$ and $\text{Threshold}_{dci\_w} = 0.2$.

4.1.3.2.2.2 Precipitating Cloud Test

The Precipitating Cloud Test exploits the reflective nature of thick ice clouds at 3.7 μm. Optically thick ice clouds, such as towering cumulonimbus, reflect more strongly than optically thin cirrus. Therefore, the brightness temperature from channel 3, T_{B3}, is much higher than the true physical temperature of clouds, represented by T_{B4}. The test is defined as

$$T_{B3} - T_{B4} > \text{Threshold}_{\text{precip(1)}} \tag{4.1-8}$$

where $\text{Threshold}_{\text{precip(1)}} = 20.0$ K is a cloud detection threshold.

Two additional checks should also be performed to discriminate cumulonimbus clouds from low liquid water clouds and optical thin ice clouds, such as cirrostratus.

$$T_{cs} - T_{B4} > \text{Threshold}_{\text{precip(2)}} \tag{4.1-9}$$

$$\rho_1 > \text{Threshold}_{\text{precip(3)}} \tag{4.1-10}$$

where T_{cs} is the clear sky brightness temperature, ρ_1 is reflectance of AVHRR channel 1, and $\text{Threshold}_{\text{precip(2)}}$ and $\text{Threshold}_{\text{precip(3)}}$ are precipitating cloud detection thresholds. $\text{Threshold}_{\text{precip(2)}} = 30.0$ K and $\text{Threshold}_{\text{precip(3)}} = 0.45$.

The $T_{cs} - T_{B4}$ test eliminates any low clouds that pass the $T_{B3} - T_{B4}$ test by ensuring that the true physical cloud top temperature is significantly lower than the clear scene brightness temperature. The ρ_1 test eliminates ice clouds that are not optically thick, and hence not as bright as precipitating clouds.

4.1.3.2.2.3 Low Cloud and Fog Test

The Low Cloud and Fog Test is based on the different radiative characteristics of liquid water clouds at AVHRR channel 3 (3.7 μm) and channel 4 (10.8 μm) wavelengths. During daytime, the radiance from channel 3 is a combination of both emitted and reflected energy, while channel 4 is only emitted energy. The test assumes that a liquid water cloud will reflect enough solar energy at 3.7 μm to make the channel 3 brightness temperature, T_{B3}, significantly higher that T_{B4}. The test is defined as the difference between the 3.7- and 10.8-μm brightness temperatures (BTD_{34}):

$$T_{B3} - T_{B4} > \text{Threshold}_{lcf} \tag{4.1-11}$$

where Threshold_{lcf} is a surface-dependent cloud detection threshold given in Table 4.1-6.

The test is extremely sensitive to desert surface and Sun glint, since they increase the 3.7-μm radiance relative to the 10.8-μm radiance. Potential sun glint areas are identified prior to testing for cloud

Table 4.1-5.

Surface background	Threshold (K)
Nondesert	12.0
Desert	20.0

contamination. When sun glint becomes increases reflectance more than a few percent, the PH classifier is used instead of a threshold test.

4.1.3.2.2.4. Reflectance Threshold Test

The test described here is used in CLAVR, SERCAA, and ISCCP, and uses a visible wavelength channel threshold to discriminate cloud (typically having high reflectances except for thin cirrus) from backgrounds having relatively low reflectances. This test is not optimal for determining cloud cover over snow- or ice-covered surfaces or in regions of sun glitter over water surfaces. The clear sky background reflectance (ρ_{cs}) is calculated from clear sky albedo (α_{cs}) and the bidirectional reflectance function (BDRF). The clear-sky albedo is obtained by spatial and temporal interpolation from ISCCP's 3-hour 2.5° map. The BDRF's for ocean and land were developed from GOES East and GOES West data (Minnis and Harrison 1984a, b, c); BDRF's for other surface types are taken from the ERBE broadband bidirectional models until other models can be developed and tested.

The clear sky reflectance is shown as follows:

$$\rho_{cs} = \alpha_{cs} / \mathrm{BDRF}(\theta_o, \theta, \phi, M) \tag{4.1-12}$$

where θ_o, θ, and ϕ are solar zenith, viewing zenith, and relative azimuth angles, and M is scene type.

A pixel is classified as cloudy if the satellite measured reflectance exceeds the expected clear-scene background value by an amount greater than a threshold. The test is only applied for the pixels with $\theta_o < 70°$ and not applied for regions containing sun glint, desert, or snow/ice background. Separate thresholds and different channels are used for land and water backgrounds. The test is defined as

$$\rho_1 - \rho_{cs} > \mathrm{Threshold}_{\mathrm{land}} \quad \text{(Over land)} \tag{4.1-13}$$

$$\rho_1 - \rho_{cs} > \mathrm{Threshold}_{\mathrm{water}} \quad \text{(Over water)} \tag{4.1-14}$$

where $\mathrm{Threshold}_{\mathrm{land}} = 0.14$ and $\mathrm{Threshold}_{\mathrm{water}} = 0.08$ are cloud detection thresholds over land and water background, respectively.

4.1.3.2.3 Nighttime Analysis

4.1.3.2.3.1 Low Stratus Test

Both SERCAA and CLAVR describe low stratus tests (LST) based upon the brightness temperature differences between the 3.7- and 11-μm channels. The test assumes that for water droplet clouds, the emissivity at 3.7 μm (channel 3) is general lower than at 10.8 μm (channel 4). For the CLAVR test, the threshold for the LST test ($\mathrm{Threshold}_{LST}$) is described as:

$$\mathrm{Threshold}_{LST} = \exp\{A + BT_{B4}\} - C \tag{4.1-15}$$

where $A = -9.37528$, $B = 0.0341962$, and $C = 1.0$ (oceans) and $C = 3.0$ (land). The constant C increases for land from the ocean value and depends on surface type. This test is applicable for the temperature range 264 K to clear-sky T_{B4}. If the threshold is exceeded, then low stratus is said to exist. The specific

values of the coefficients may vary in the CERES implementation, depending on the results of testing with global GAC data.

The SERCAA test assumes that clouds are detected if T_{B4} is greater than T_{B3} by an amount greater than a cloud detection threshold:

$$T_{B4} - T_{B3} > \text{Threshold}_{LST} \tag{4.1-16}$$

where Threshold_{LST} is a surface-dependent cloud detection threshold:

$$\text{Threshold}_{LST} = 1.0 \text{ K} \qquad \text{(Over nondesert)}$$

The final determination of thresholds to use for the CERES algorithm will be determined through global analysis of AVHRR data. Further work is underway to refine the threshold over various surface types.

Extensive comparisons were performed between the CLAVR and SERCAA tests. There was little difference between the results of application for the two tests. Since the CLAVR test uses an exponential equation that requires more CPU time than the simple brightness temperature threshold used in the SERCAA test, the SERCAA test is chosen for the CERES code.

4.1.3.2.3.2 Thin Cirrus Test

Both the SERCAA and CLAVR methods use a similar test based upon the difference in brightness temperatures between the 3.7- and 12-micron channels ($T_{B3} - T_{B5}$, or BTD_{35}). The test is based on the idea that cirrus cloud transmissivity at 3.7 μm (channel 3) is generally greater than at 12 μm (channel 5), causing some radiation from warmer backgrounds to be included in the channel 3 measurement. If the difference exceeds a given threshold, then cirrus is said to exist in the pixel.

The SERCAA Nighttime Thin Cirrus Cloud Test is defined as:

$$T_{B3} - T_{B5} > \text{Threshold}_{tci} \tag{4.1-17}$$

where Threshold_{tci} = 4.0 K is the nighttime thin cirrus cloud detection threshold. Tests are still underway to determine the best implementation of the threshold test.

4.1.3.3 Cloud discrimination in complex regions

The discrimination between clouds and clear-sky is performed typically by applying a single threshold test at a time in a predetermined sequence. As a result of feedback from the Surface and Atmospheric Radiation (SARB) group, however, the intended purpose of the cloud mask has changed quite dramatically over the past six months. Besides wanting information on whether cloud is present or not, the SARB group also wants information on whether smoke, fires, snow, sea ice, or sunglint is present in the pixel. As a result of this feedback and the growing necessity to expand the utility of the cloud mask, it became necessary to derive a new approach to cloud discrimination. The basic idea of the following discussion is the development of modules that group simple threshold tests instead of applying tests individually in some sequential fashion. The basic threshold tests to detect cloud are quite similar to those described in the previous section. Additional tests have been developed to further discriminate between cloud and smoke, cloud and sunglint, cloud and fire, cloud and snow, and cloud and sea ice.

At the time of this writing, modules have been developed for several complex regions, specifically sunglint over water, clouds over snow/sea ice, and biomass burning areas over forest. Feedback from the SARB group has been positive as has been independent testing of these tests by the MODIS cloud mask group at the Space Science Engineering Center (SSEC) at University of Wisconsin, Madison. Other modules are currently in development for nighttime discrimination between clouds and snow/sea

ice, smoke over IGBP surface types other than forest, and over mountains. These new modules will be developed, tested, and incorporated as time permits.

4.1.3.3.1 Determination of clouds in sunglint regions

The discrimination between clouds and clear-sky in sunglint regions over water is necessary when working with AVHRR data with both morning and afternoon orbiters. In AVHRR Global Area Coverage (GAC) imagery over oceans, sunglint is readily apparent in about 25-30% of the data. Since the visible and near-infrared channels are affected by the increased solar reflectance in sunglint regions, tests that use these channels generally do not perform well.

There are two conditions that need to be met before the sunglint module may be applied. First, the pixel must be over water. Second, a sunglint probability is calculated based upon knowledge of the viewing geometry (solar zenith angle, viewing zenith angle, and relative azimuth angle) using the approach detailed by Cox and Munk (1954). The sunglint probability curves are based upon surface wind speed, and thus ocean surface roughness, but for our purposes we simply adopt one set of curves until we have a method to estimate surface ocean roughness.

Our approach in sunglint regions is somewhat different than the conventional threshold masking approach used in previous sections; namely, to apply a threshold test one at a time. Our sunglint test is composed of six tests applied in a specific order; each test contains one or more individual threshold tests. Each pixel undergoes all the following tests in sequence. Even if a pixel is designated as a cloud in one of the first tests, it may be changed to sunglint in a subsequent test.

1. This first test will paint almost all of the pixels in the sunglint region as containing cloud. The remaining tests will overwrite the result of this first test if the stated conditions are true.

If $[(T_{B3}-T_{B4}) > 15 \;\&\&\; (\rho_1 > 0.2) \;||\; (T_{B4}-T_{B5}) > 1.0\;]$, then pixel contains cloud.

2. This is a cold cloud test - if the clouds in the sunglint region are below about 250K, the 3.7-micron brightness temperature will not be saturated at 320K.

If $[T_{B3} < 303.0 \;\&\&\; \rho_1 > 0.10]$, then the pixel contains cloud.

3. This next test seems to do well at masking low-level clouds in sunglint regions; it may be redundant.

If $[(T_{B4}-T_{B5}) > 2.75]$, then the pixel contains cloud.

4. This test is for low to moderate sunglint. If this condition passes, the implication is that there is no cloud and that there is some enhancement of visible reflectance over open water. The result of this test overwrites previous results.

If $[(\rho_3/\rho_1) > 0.7 \;\&\&\; \rho_1 >= 0.10\;]$, then the pixel is not cloudy but contains low to moderate enhanced reflectivity due to sunglint.

5. This test is for extremely high sunglint. If this condition passes, the implication is that there is no cloud and that the 3.7-micron channel is saturated. The result of this test overwrites previous results.

If $[T_{B3} = 320.0 \;\&\&\; \rho_1 >= 0.24\;]$, then the pixel is not cloudy and contains extreme sunglint.

6. If an imager pixel passes this test, there is no cloud and the the reflectance of the water is lower than expected for sunglint conditions. This could be due to wind ruffling the water, for instance. The result of this test overwrites any previous result.

If $[(T_{B3}-T_{B5}) < 14.0$ && $\rho_1 < 0.13]$, then the pixel is not cloudy but has a much lower reflectance than expected in a sunglint region

Figure 4.1-1 provides some idea of how these simple threshold tests work on an image recorded on 1 October, 1986 over the western Pacific Ocean north of Australia. The left frame shows a false color image in which clouds appear as white, clear ocean is dark, and vegetated land is green. Note the region of sunglint (enhanced reflectivity) in the image. The right frame shows the results from application of the threshold tests. Only the area denoted as containing a significant probability of sunglint (> 5%) according to the Cox and Munk (1954) relationship is analyzed using this set of threshold tests; the rest of the image is unprocessed.

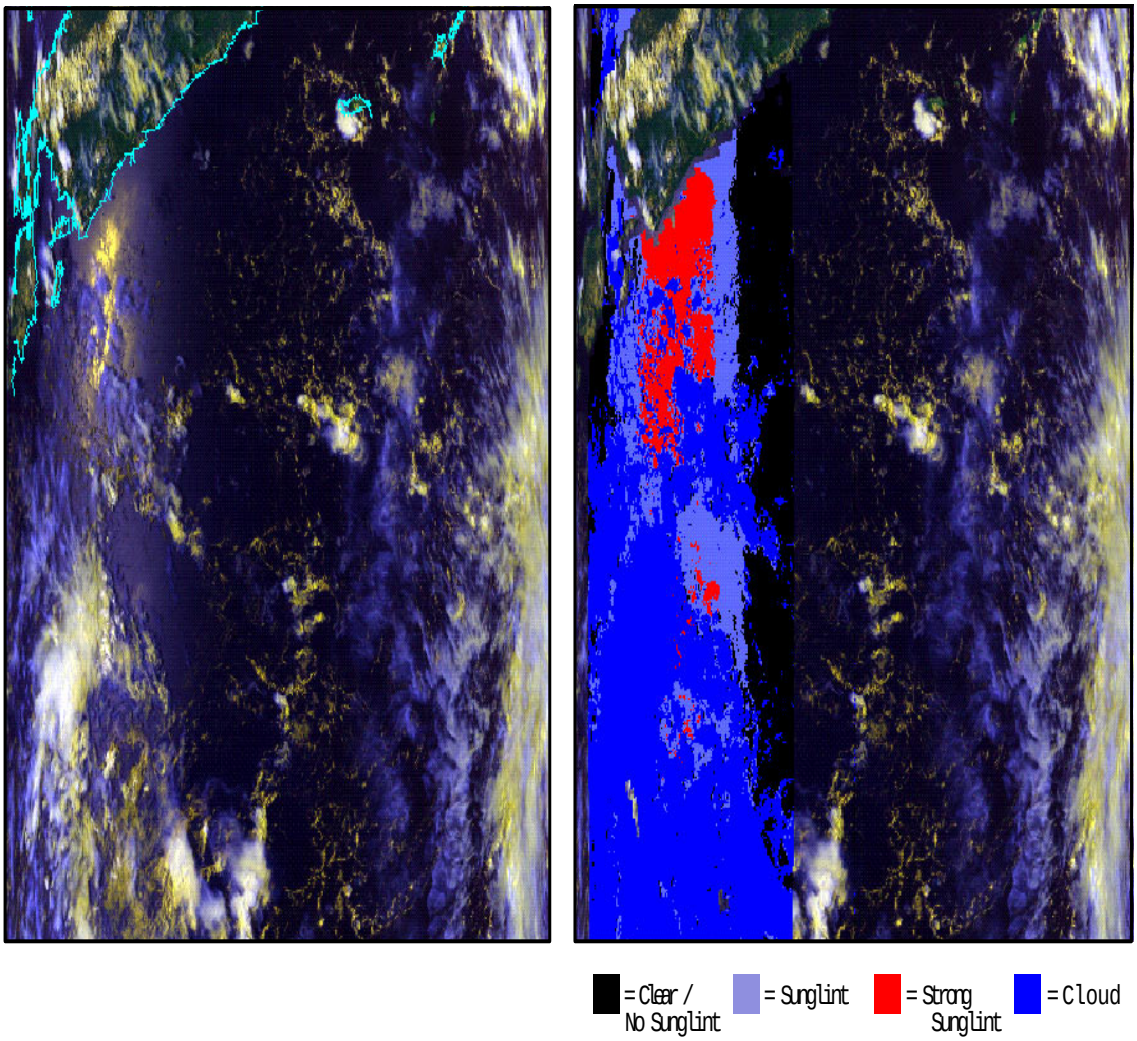

Figure 4.1-2. False color image (left frame) derived from 4-km AVHRR GAC data collected by NOAA-9 for 1 October, 1986. Sunglint appears in left half of image. In the right-hand frame, data are analyzed using the sunglint module described in Section 4.1.3.3.1.

4.1.3.3.2 Determination of clouds in regions containing surface snow or ice. One of the more important advances we will make between the ERBE and CERES products is in better discrimination between clouds and surface snow/ice in high elevation and high latitude regions. The radiation budget of snow- and ice-covered regions is dominated by radiation throughout most of the year. At the top of the atmosphere (TOA), high latitudes are net losers of energy except near the summer solstice, thereby balancing the net surplus of energy in lower latitudes. Clouds play a relatively small role in governing fluxes at the TOA at high latitudes. They have little impact on the planetary albedo over the already bright surface, so solar cloud forcing is small. In the infrared region of the spectrum they also have relatively little effect because the clouds are often low and trapped beneath near-surface temperature inversions. This results in their temperature contrast with the surface being almost nil, or even warmer than the surface.

The energy budget at the surface, however, is another story. Unlike other regions of the globe, sensible and latent heat fluxes are usually much smaller than the radiation fluxes, except near the sea ice edge in winter and during the summer melt season. During the late spring and summer solar radiation plays the leading role, while the long polar night is dominated by longwave radiation. In some respects this simplifies the picture, but these simplifications are more than offset by additional complications in detecting and characterizing clouds over snow and ice. Unfortunately, however, one cannot hope to measure surface radiation fluxes from space without knowing something about the cloud conditions.

Why do we care about the surface energy fluxes in polar regions? According to state-of-the-art global climate prediction models, the polar regions are the most sensitive regions on Earth to changes in the climate system. This is believed to be because of feedback mechanisms involving snow cover and sea ice. For example, if the climate were to warm, sea ice and snow would melt, exposing more low-albedo land and ocean so that more solar radiation can be absorbed by the surface. This in turn further warms the atmosphere, which melts more ice, which allows more absorption, etc. The problem is that many of these climate models use very crude parameterizations of energy transfer between the atmosphere and the surface, primarily because our understanding of these processes is not very good. Because few people live in high-latitude locations there are few conventional data with which to study the energy transfer. This is where satellites come in. If we can develop methods to measure the surface energy balance from the relatively high temporal and spatial resolution of satellite data, we would gain a better understanding of air/ice/sea interactions and provide better parameterizations to climate modelers. At this time, the largest obstacle in attaining this goal is being able to detect and measure clouds over snow and ice.

Our tests for discrimination between clouds and snow or sea ice will be aided by ancillary snow/ice maps provided either by NOAA or by the National Snow and Ice Data Center (NSIDC). If there is snow or ice in the swath of satellite data being processed, we will use one of two sets of tests that are based on surface temperature. The first set of tests are used over polar regions where the surface temperature is extremely cold - below 260 K. Each pixel undergoes all the following tests in sequence. Even if a pixel is designated as snow/sea ice one of the first tests, it may be changed to cloudy in a subsequent test.

1. if [(ρ_3/ρ_1) <= 0.06 || (ρ_1 >= 0.25 && ρ_3 <= 0.05 && (T_{B3}-T_{B4}) <= 16.)], then the pixel is not cloudy but contains snow or ice
2. if [(b3-b4) >= 8.0 && ρ_3 >= 0.055 && (ρ_3/ρ_1) >= 0.07], then pixel is cloudy.

The second set of tests are used over polar regions where the surface temperature is between 260 K and 277 K.

3. if ((ρ_1 >= 0.2) && (b4 <= 277.) && (ρ_3 <= 0.03) && ((T_{B3}-T_{B4}<=8.)), then the pixel is not cloudy but contains snow or ice.

4. if ((T_{B3}-T_{B4}) > 8. && (ρ_3 > 0.05) || (T_{cs}-T_{B4}>=12), then the pixel is cloudy.

Figure 4.1-2 provides some idea of how these simple threshold tests work on an image recorded on 28 November, 1991 over the central United States (Wyoming and Montana). In this image, clouds are white, snow is yellow, and clear land is dark. Fresh snow covers most of Wyoming and Montana. Surface synoptic observations from Billings, Montana note the presence of surface snow and also the presence of cirrus and altocumulus. In Casper, Wyoming, surface synoptic observations also report snow on the ground and additionally the presence of cirrus and stratocumulus. The right frame provides an indication of how the module works for discriminating between clouds and snow. For the most part, the algorithm performs well with the main confusion being caused by cloud shadows and cloud edges.

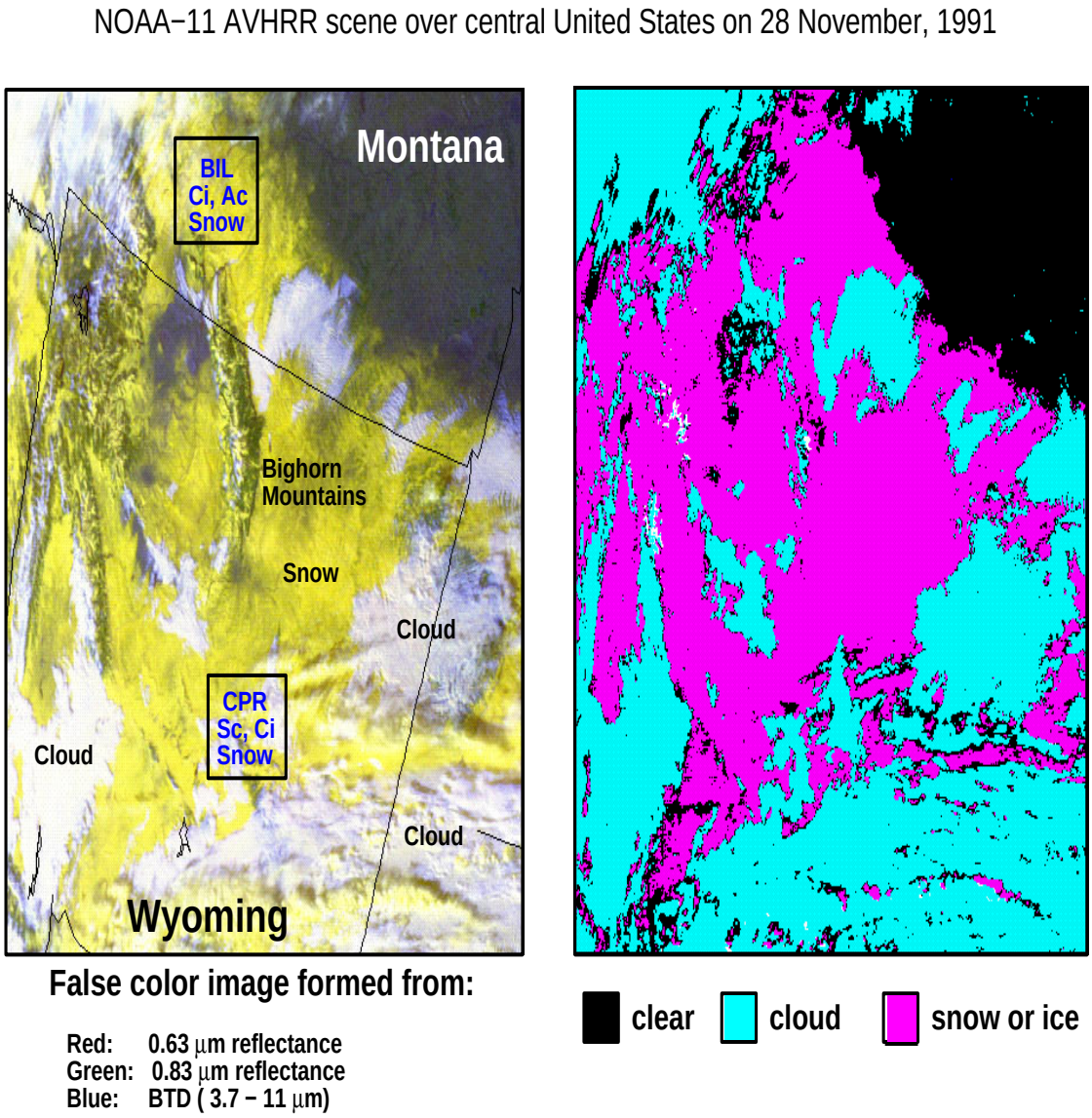

Figure 4.1-3. False color image (left frame) derived from 1-km AVHRR LAC data collected by NOAA-11 for 28 November, 1991. In the left frame, clouds are white, snow appears as bright yellow, and clear land is dark (e.g., upper right corner of image). In the right-hand frame, data are analyzed using the snow module described in Section 4.1.3.3.2.

4.1.3.3.3 Discrimination of clouds from smoke and fires over forested regions.

The amount of biomass burning is often overlooked in satellite data analyses. The majority of large scale biomass burning occurs in forests (tropical, temperature, and boreal), savannas, and agricultural lands after the harvest (e.g., Levine et al. 1995). From satellite data, however, savannah fires and smoke are much harder to detect than boreal forest fires due to the amount of material being burned. Boreal forests burn hotter than savannah fires because there is so much more material to be consumed in the form of trees than in grassland. It is often the case that forest fires are large enough to be present in AVHRR satellite data, both at 1-km and 4-km resolution. In our use of October 1986 AVHRR/ERBE data for the development of the cloud subsystem code, it quickly became apparent that extremely large fires and smoke plumes were present over eastern Siberia, with smoke plumes extending southward and eastward across China.

Given the importance of smoke in SARB calculations, we developed a module to discriminate between smoke, fires, and clouds in AVHRR data. The tests are confined to IGBP ecosystem types defined as forest only. Because of the difficulty in interpreting the 3.7-μm reflectances over grassland, savannah, and cropland, development of techniques to discriminate between smoke and cloud over these surface types are left to future development. Each pixel undergoes all the following tests in sequence. Even if a pixel is designated as a cloud in one of the first tests, it may be changed to smoke or fire in a subsequent test.

1. This first test is similar to the CERES cold cloud test. The temperature 273 should be replaced by the top-of-atmosphere (TOA) 11-micron brightness temperature minus some appropriate threshold.

If ($T_{B4} < 273.$), then the pixel contains cloud.

2. This test catches the clouds that display a high brightness temperature difference between the 3.7 and 11 micron channels that also display a relatively high reflectivity in channel 1. Clouds also exhibit a relatively high value in channel 3 reflectance (ρ_3).

If ((T_{B3}-T_{B4})>6. && ρ_1 >0.12 && T_{B3}<310. && ρ_3>0.09), then the pixel contains cloud.

3. This is a fire test. Over forests, the channel 4 brightness temperature rarely exceeds 300K, and fires are mainly evident in channel 3. Sometimes the 3.7 micron channel will saturate (i.e., T_{B3}=320K) when an extremely bright cloud is present, hence the T_{B4}>275K test. The ($T_{B4} > 276$) test should be replaced with a surface brightness temperature based upon some gridded meteorological product such as NCEP, DAO, or ECMWF.

If ($T_{B3} > 315.$ && (T_{B3}-T_{B4}) > 10. && T_{B4}>276.), then the pixel contains fire.

4. This is the actual smoke test. First, the channel 1 reflectivity is set approximately 6% above the usual background forest reflectivity which usually does not rise above about 0.09 at any viewing angle (usual range: .04-.07). The next condition (ρ_1 <=0.35) was put in once we discovered that most smoke, no matter how thick, usually does not exceed this reflectance. On the other hand, most clouds greatly exceed this reflectance threshold. The third test (ρ_3<=0.035) was added because most smoke shows very little brightness temperature difference (BTD) between 3.7 and 11 microns, hence the channel 3 reflectivity is usually very low. The fourth test (T_{B3}-T_{B4})<=5 may be redundant in light of the previous test. We have noticed, however, that on some occasions, thick smoke will exhibit BTD's greater than 5C. Why? It could have to do with intense convection occurring directly over the burn site. The final

test (T_{B4}>276) was added to address a specific problem. Extremely bright clouds (e.g., 270K) can be so reflective at 3.7 microns that the T_{B3} saturates at 320K. While the pixel is clearly cloud, the fire test can be fooled unless an attempt is made to remove bright clouds first. The 276K threshold should be replaced with a TOA brightness temperature (11 micron) based upon temperature and humidity profiles.

If (ρ_1 >0.13 && ρ_1 <=0.4 && ρ_3<=0.035 && (T_{B3}-T_{B4})<=5. && T_{B4} >276.), then the pixel contains smoke.

Figure 4.1-3 provides some idea of how these simple threshold tests perform on an image recorded on 23 July, 1989 over Manitoba, Canada. This scene is extremely complex and shows a severe outbreak of forest fires with associated smoke plumes. A front is passing through the center of the image. Note that the smoke plumes indicate windier conditions ahead of the front (to the right of the cloud band). At the bottom of the image, note the presence of cumulus cloud streets. The smoke/fire/cloud discrimination tests do not confuse smoke with cloud, or fire with cloud. However, as noted from the right frame, some confusion may be caused around cloud edges when smoke is present (e.g., see cloud streets at bottom of image).

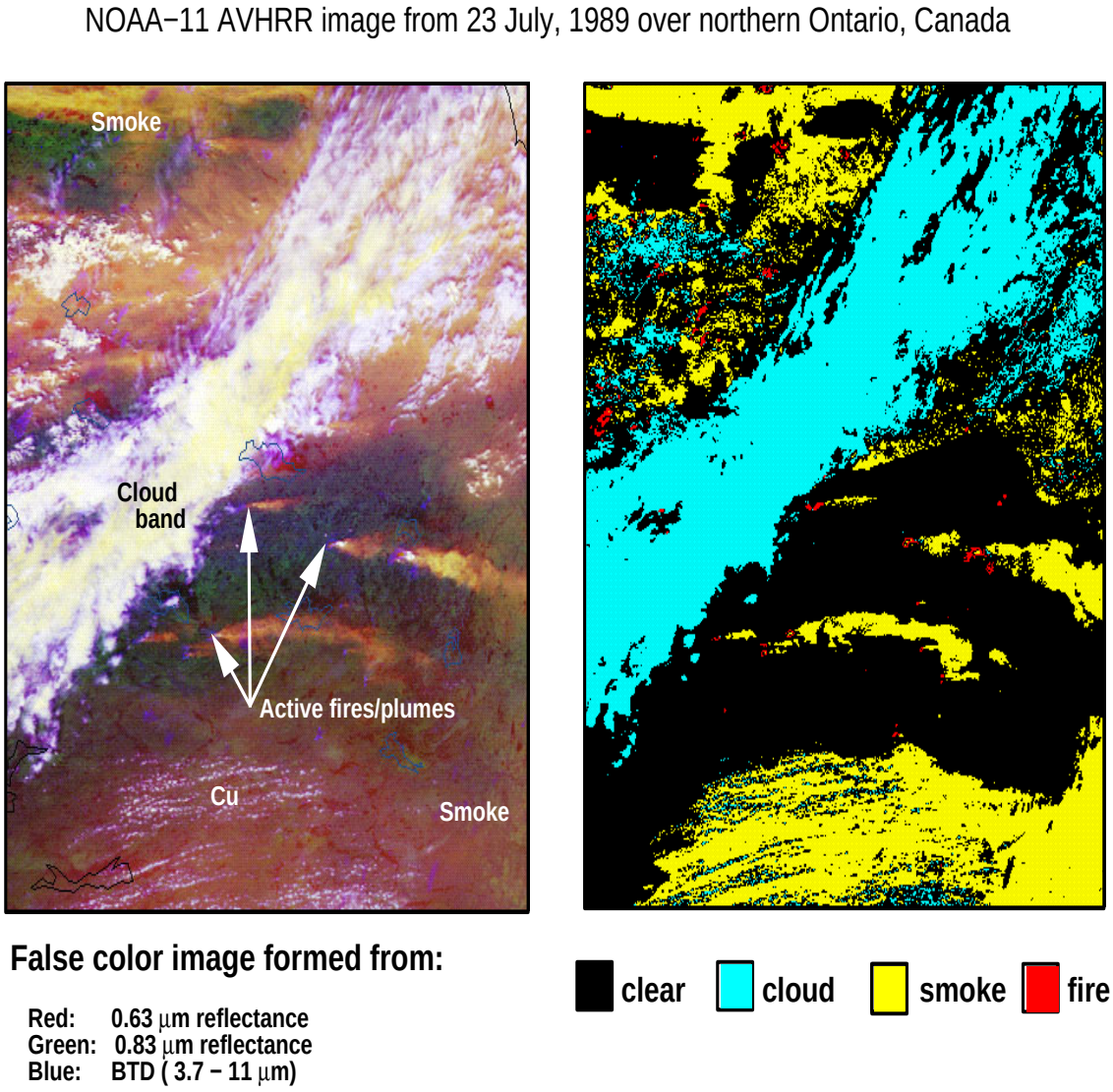

Figure 4.1-4. False color image (left frame) derived from 1-km AVHRR LAC data collected by NOAA-1 for 23 July, 1989 over Manitoba and northern Ontario, Canada. The discrimination between clouds, smoke, fires, and clear sky conditions is performed using the module described in Section 4.1.3.3.3.

4.1.3.3.4 Discrimination of clouds in desert regions.

Cloud discrimination in desert regions is difficult when the surface becomes extremely hot and the satellite NIR and IR radiances are close to their upper detection limit. The SARB group has requested that clouds be separated from clear-sky and dust storms. However, in practice, we have been able to discriminate between only clouds and clear-sky with some degree of accuracy. Dust storms are extremely difficult to discern because of the loss of all texture in the image.

The assumption is made that all pixels are clear unless cloud is detected. The cloud detection tests are applied as follows:

If $((T_{B3}-T_{B4}) > 17.)$ or $((\rho_l - \rho_{cs}) > 0.05$ && $(T_{cs} - T_{B4}) > 10.))$, then the pixel contains cloud.

In future revisions, we hope to be able to discriminate between clear sky and dust storm conditions.

4.1.4. Short-Term and Long-Term Clear-Sky Composite Maps

4.1.4.2. Clear-Sky Composite Maps

The ISCCP developed clear-sky reflectance and temperature composites to detect clouds over a given 32-km square area by comparing the pixel radiances to the clear-sky composite values with some added thresholds (Rossow and Garder 1993). These composites are based on the observation that variations in VIS clear reflectances usually are smaller in time than in space, especially over land. Variations of surface VIS reflectances generally are smaller than variations of cloud reflectances. Therefore, it is assumed that the characteristic shape of the darker part of the VIS radiance distribution is at most weakly dependent upon surface type (Seze and Rossow 1991a, b). The minimum reflectance value for channel 1 is used to estimate clear values. Corrections to the minimum values are inferred from the shapes of the visible reflectance distribution associated with different surface types.

Rossow and Garder (1993) classify the surface into nine types depending on the time scale and magnitude of the reflectance variations. The clear sky reflectance values for land and ocean regions whose surface characteristics vary the most rapidly are estimated using short-term values of ρ_{min} such that $\rho_{cs} = \rho_{min}(ST) + DEL2$. Sparsely vegetated surfaces generally exhibit more spatial variability than heavily vegetated surfaces (cf. Matthews and Rossow 1987), but are also generally less cloudy. For these, $\rho_{cs} = \rho_{min}(LT) + DEL2$. Vegetated areas show less small-scale spatial variability. They also tend to be more uniform from one geographic location to another. For vegetated regions, the clear-sky reflectance is determined by first calculating $\rho_{cs} = \rho_{min}(ST) + DEL2$. Then the individual pixel reflectance values within each latitude zone are compared to the distribution of ρ_{cs} values for the same ecosystem type; they are required to be within DEL1 of the distribution mode value, ρ_{mode}.

Similar assumptions are used for the determination of T_{cs} fields. The time scales of VIS and IR variability for different classes and the associated ISCCP thresholds are shown in Tables 4.1-8 through 4.1-11.

Table 4.1-6.

VIS classes	Short term (ST)	Long term (LT)
Ocean	-	30 days
Lakes	-	15 days
Polar ocean (open water)	-	15 days
Ice-covered water	5 days	-
Forests, woodlands, shrublands	-	30 days
Grasslands, tundra	-	30 days
Arid vegetation, deserts	-	30 days
Polar land (snow free)	-	15 days
Snow- or ice-covered land	5 days	-

Table 4.1-7.

IR surface types	DEL1	DEL2
Ocean, near-coastal, lakes	3.0	1.5
Forests, woodlands, shrubland	6.0	3.5
Grasslands, tundra	-	3.5
Arid vegetation, deserts	-	3.5
Ice-covered water	-	5.0
Ice- or snow-covered land	-	5.0

Table 4.1-8.

IR classes	Short term (ST)	Long Term (LT)
Open ocean	15 days	30 days
Near-coastal ocean and lakes	5 days	15 days
Polar seas and ice-covered water	5 days	15 days
Land	5 days	15 days
High and rough topography land	5 days	15 days
Ice- or snow-covered land	5 days	15 days

Table 4.1-9.

IR surface types	DEL1	DEL2	DEL3
Ocean	2.0	2.0	2.5
Near-coastal ocean, lakes	3.0	3.0	4.0
Ice-covered water	3.0	3.0	4.0
Land	6.0	5.0	8.0
High and rough topography	9.0	7.0	11.0
Ice- or snow-covered land	9.0	7.0	11.0

One of the primary difficulties in using the ISCCP approach as currently formulated is the angular dependence of clear-sky reflectance. Although cross-track scanning Sun-synchronous satellites such as the NOAA-AVHRR repeat the angular viewing conditions on a regular cycle, the solar zenith angle slowly varies and the cloudiness conditions may prevent the determination of clear-sky reflectance at some points in cycle. The ISCCP relies on an empirical bidirectional reflectance model for clear-sky ocean reflectance (Minnis and Harrison 1984a). Thus, over ocean, the angular problems are minimized. Over land, the ISCCP assumes isotropic clear-sky reflectance, although it has been established that the anisotropy of land scenes is significant (e.g., Kriebel 1978; Tarpley 1979; Minnis and Harrison 1984c; Suttles et al. 1988). For $\theta_o < 85°$, the vegetated land clear-sky anisotropic reflectance factor $R(k, \theta_o, \theta, \phi)$, where k is a surface type that can vary from 0.6 to 1.6 (e.g., Suttles et al. 1988) for $\theta < 70°$. Thus, there is the potential for clear-sky reflectance errors as great as 300% if one assumes that the measurement taken at a particular set of viewing conditions represents the reflectance at all viewing angles for a given value of θ_o. Systematic changes of albedo with θ_o are also not considered for land surfaces. The reflectance anisotropy over snow and desert scenes is generally not as great as that over vegetated surfaces, but the absolute changes in reflectance are as great because of the higher albedos over these surfaces.

The CERES processing will begin with a set of global clear-sky radiances matched to a 10-min database at a 3-hourly resolution. Thus, a relatively high-resolution clear-sky field is required. The clear-sky radiance maps currently available from the ISCCP are the C1 datasets that have a 250-km and 3-hour resolution and that lack the anisotropy corrections noted above. The following processing steps using the ISCCP data are applied to historical AVHRR data to obtain the clear-sky radiances at the higher spatial resolution and to account for reflectance anisotropy.

From the ISCCP C1 data, the clear-sky reflectance at a given day d, synoptic hour h, nominal regional latitude Θ_{C1}, and longitude Φ_{C1} is $\rho_{csC1}(\theta_o, \theta, \phi, \Theta_{C1}, \Phi_{C1}, h, d)$. The corresponding clear-sky albedo is

$$\alpha_{csC1}(k, \theta_o, \Theta_{C1}, h, d) = \frac{\rho_{csC1}(k, \theta_o, \theta, \phi, \Theta_{C1}, \Phi_{C1}, h, d)}{R(k, \theta_o, \theta, \phi)} \quad (4.1\text{-}18)$$

where the value of R is taken from Minnis and Harrison (1984a) for vegetated land and from Suttles et al. (1988) for snow and desert. Over ocean, α_{csC1} is estimated using an updated version of the clear

ocean bidirectional reflectance model of Minnis and Harrison (1984a). The updated version includes calibrated data from more angles than the original model. The value of α_{csC1}(ocean, $\theta_o = 0$) = 0.045. The standard deviation of α_{csC1} is $\sigma_{\alpha C1}(k, \theta_o, \theta, \Theta_{C1}, \Phi_{C1}, h, d)$. For mixed land-water regions, the reflectance for the land portion is, leaving off the dependence on the parameters θ_o, θ, ϕ, Θ_{C1}, Φ_{C1}, h, and d:

$$\rho_{csC1}\,(\text{land}) \;=\; \frac{[\rho_{csC1} - (1 - f_{\text{land}})\,\rho_{csC1}\,(\text{ocean})\,]}{f_{\text{land}}} \tag{4.1-19}$$

where f_{land} is the land fraction in the $C1$ region. The standard deviation of α_{csC1} is $\sigma_{\alpha C1}(k, \theta_o, \theta, \Theta_{C1}, \Phi_{C1}, h, d)$. Average values of these parameters, $<\alpha_{csC1}(k, \Theta_{C1}, \Phi_{C1}, h)>$ and $<\sigma_{\alpha C1}(k, \Theta_{C1}, \Phi_{C1}, h)>$ are computed for each region and month.

The corresponding ISCCP clear-sky, 11-μm temperatures and their standard deviations are $T_{csC1}(k, \Theta_{C1}, \Phi_{C1}, h, d)$ and $\sigma_{TC1}(k, \Theta_{C1}, \Phi_{C1}, h, d)$, respectively. Monthly mean values, $<T_{csC1}(k, \Theta_{C1}, \Phi_{C1}, h)>$ and $<\sigma_{TC}(k, \Theta_{C1}, \Phi_{C1}, h)>$, are also computed for these parameters. All 10-min regions falling within the 250-km $C1$ region are initially assigned the clear-sky radiances for the ISCCP region if the $C1$ region is all land or water. If the $C1$ region is mixed, the 10-min boxes that are entirely water are assigned the empirical model values for ocean albedo and the land boxes are given the land clear-sky albedos computed from (4.1-24) and (4.1-25). The coastal boxes retain the nominal $C1$ albedo. The $C1$ temperature is assigned to the 10-min box regardless of the geotype. These mean values constitute the starting point for the development of the high-resolution clear-sky radiance set.

To derive the high-resolution dataset, AVHRR GAC data are analyzed to determine if the pixels belonging to a particular 10-min box are clear. During a given AVHRR orbit at time t, the reflectance ρ, and 11-μm brightness temperature T_{B4} of all pixels located within a given 10-min box are compared to the monthly mean dataset. The pixels are assumed to be clear if, again leaving off the dependence on the parameters k, θ_o, θ, ϕ, Θ_{C1}, Φ_{C1}, h, and d:

$$\rho\,(t) < \rho_{csC1}\,(t) + 2\sigma_{\alpha C1} \tag{4.1-20}$$

and

$$T_{B4} > T_{csC1} - 2\sigma_{TC1} \tag{4.1-21}$$

where $h < t < h + 1$, and

$$\rho_{csC1}\,(k, \theta_o, \theta, \phi, \Theta_{C1}, \Phi_{C1}, t) \;=\; R\,(k, \theta_o, \theta, \phi)\,\alpha_{csC1}\,(k, \theta_o, \Theta_{C1}, \Phi_{C1}, t) \tag{4.1-22}$$

The last term in (4.1-28) is the albedo at time t found by linearly interpolating the $C1$ albedos in time. First, the albedos are extended to θ_o using the directional reflectance models derived from the results of Minnis and Harrison (1984a, c) based on the mean θ_o at the synoptic times. This approach is the same employed by the ERBE time-space averaging subsystem (see Brooks et al. 1986). Simple linear inter-polation is used to determine the expected standard deviation. When albedos do not exist at h or $h + 1$, the available albedo is extrapolated to t using the directional reflectance models. Over snow scenes, additional tests using the $T_{B3} - T_{B4}$ differences supplement the standard clear-sky tests to insure that the scene is cloud free. The expected clear-sky temperature, $T_{csC1}(k, \theta_o, \Theta_{C1}, \Phi_{C1}, t)$ and its standard deviation are interpolated using linear interpolation.

For some areas, such as deserts, the surface emittance at 3.7 μm will not be unity. When the surface emittance is less than unity, the task of determining the expected clear-sky 3.7-μm brightness temperature will be difficult. For this reason, we will develop a surface emittance map at 3.7 μm using nighttime data so that there is no solar contribution. The effective surface emittance ε_{3s} for channel 3 is also estimated for each 10-min box by first correcting the nighttime clear-sky values of T_{B3} and T_{B4} for water

vapor attenuation. Assuming that the clear-sky downwelling radiance is zero for channel 3 and $\varepsilon_{4s} = 1$, then $\varepsilon_{3s}s = [B_3(T_{B4s}) - B_3(T_{B3s})] / B_3(T_{B4s})$, where the subscript *s* indicates values at the surface.

The pixel values selected as clear are then analyzed as in Minnis et al. (1987) to determine an estimate of ρ_{cs} and T_{cs} for the 10-min box and new values for their standard deviations. The procedure is reversed to estimate the clear albedo and temperature at the nearest synoptic hour. These new values plus the mean channel-3 emittances are then used to construct a new clear-sky map. The results from different days at a given *h* are averaged to yield the new detailed clear-sky fields that will become the initial CERES clear-sky radiance fields.

Examples of applying this procedure to a day of October 1986 NOAA-9 AVHRR data are shown in Figs. 4.1-6–4.1-9. The initial clear-sky reflectance field based solely on the ISCCP land "albedos" and the ocean reflectance model have a somewhat blocky appearance due to the low-resolution of the *C*1 dataset. The scattering of some of the data values near the orbit overlaps is due to overwriting of previous results by pixels in the following orbit. The ocean model produces a realistic pattern of reflectance including the distinct sun glint areas. Application of the clear-sky procedure yields a somewhat finer resolution of various features such as the Arabian Peninsula and the Pampas region in South America. Bright areas of sun glint appear in the middle of the predicted sun glint during some orbits. Changes did not occur in many areas because of clouds. The clear-sky temperature fields (Figs. 4.1-8 and 4.1-9) show even more dramatic changes because of more local variability, especially over land.

The procedure used to produce the results in Figures 4.1-7 and 4.1.9 will be applied to the AVHRR data for months during four different seasons. Over some particularly clear areas, the resulting means for a given hour will be examined closely to determine the sensitivity of the technique to the values of *R*. New anisotropic reflectance and thermal infrared limb-darkening models will be tested as they are developed. This methodology will be continuously refined prior to the TRMM launch.

The logic employed here will be combined with the other clear-sky detection methods and with a modified version of the ISCCP approach to provide updates of clear-sky radiances during CERES on the time scales suggested in the ISCCP method. The CERES clear-sky composite relies on high-resolution data applied to a higher-resolution grid than that employed by the ISCCP. Thus, accounting for local variability becomes very important. The ISCCP thresholds that bound the clear-sky domain for a particular surface category will be used as guidelines and as default values for the CERES clear-sky composite development. The local standard deviations in the clear-sky radiances computed using the above analysis procedure on preflight AVHRR data will be used to set the thresholds for cloud detection during CERES.

The following section shows a procedure for using the clear-sky radiance map in a spatial or spatial/temporal test to determine whether ocean regions are cloud-free.

4.1.5 Tests of Cloud-Free Radiances for Ocean Regions

Over oceans, cloud-free radiances exhibit a high degree of uniformity over large spatial scales. Against this uniformity cloud contaminated pixels stand as outliers in both their local uniformity and in their multispectral radiative properties. Figure 1 illustrates the contrast between the outliers and the cloud-free radiances. The figure shows cloud-free 0.63-μm reflectivities and 11-μm radiances for the 10^o X 10^o latitude-longitude region with 10^oN and 120^oW as the southwest corner of the region. The observations are derived from 4-km AVHRR GAC data for the daytime passes of NOAA-11 over the region for March 1989. Each point in the figure gives the average radiances for all pixels identified as being cloud-free within a 60-km scale subregion of the 10^o X 10^o latitude-longitude box on a particular pass. The radiances are given as functions of the satellite zenith angle: positive angles are for radiation emitted and reflected in the direction of forward scattering for the incident sunlight; negative angles are

for the backscattering direction. Because the NOAA satellites are in sun synchronous orbits, for a given latitude band and time of year, each satellite zenith angle is associated with a limited range of solar zenith and relative azimuth angles. The 60-km scale subregions used in this example are about twice the size of a CERES field of view. Clearly, similar diagrams could be created by taking the cloud-free MODIS or VIRS pixels within each CERES field of view.

The only criteria used to select the cloud-free pixels in this example is the spatial uniformity exhibited by both the reflected and emitted radiances. The clustering of the observed radiances clearly portrays the patterns of limb darkening in the infrared and sun glint in the reflected sunlight. Outliers, which probably contain significant cloud contamination, are readily detected.

The screening of cloud-free observations for ocean regions can be automated. Figure 2 illustrates the performance of simple models for limb darkening and reflected sunlight. The models are based on the observations shown in Figure 1. For limb darkening the emission is taken to be given by

$$I(\theta) = A + \frac{B}{\cos(\theta)} \tag{4.1-23}$$

where θ is the satellite zenith angle. Away from the sun glint, reflected sunlight follows a parameterization of reflectivities obtained with a plane-parallel radiative transfer model for cloud-free scenes. The reflectivity is taken to be given by

$$\rho(\theta) = \frac{1}{(\alpha + \beta\cos\theta)} \tag{4.1-24}$$

In the sun glint region the reflectivities are taken to be a gaussian function of the difference between the incident and reflected angles of the sunlight. The difference is given by

$$\cos\psi = \sin\theta\cos\theta_o\cos\psi + \cos\theta\cos\theta_o \tag{4.1-25}$$

where θo is the solar zenith angle and ψ is the relative azimuth angle. The sun glint is taken to be the domain $\psi < 30^o$.

The solid curves in the figure give the best-fit model representation of the emitted and reflected radiances. The dashed curves give one standard deviation of the observations away from the observed mean at the particular satellite zenith angle. The ragged appearance of the model fits reflects the actual ensemble of satellite zenith, solar zenith and relative azimuth angles at which the cloud-free pixels were observed. For comparison, the +'s are the means for the observations. The departure of the means from the best-fit curves illustrate the fidelity of the models in reproducing the observations. While these models can easily be improved, they perform remarkably well despite their simplicity. Validation of cloud-free radiances is accomplished by comparing the distribution of observed radiances with those predicted by the model. For example, approximately 90% of the cloud-free radiances should fall within

two-standard deviations of the predicted means. Significant departures of the distributions from the expected populations would force corrective measures.

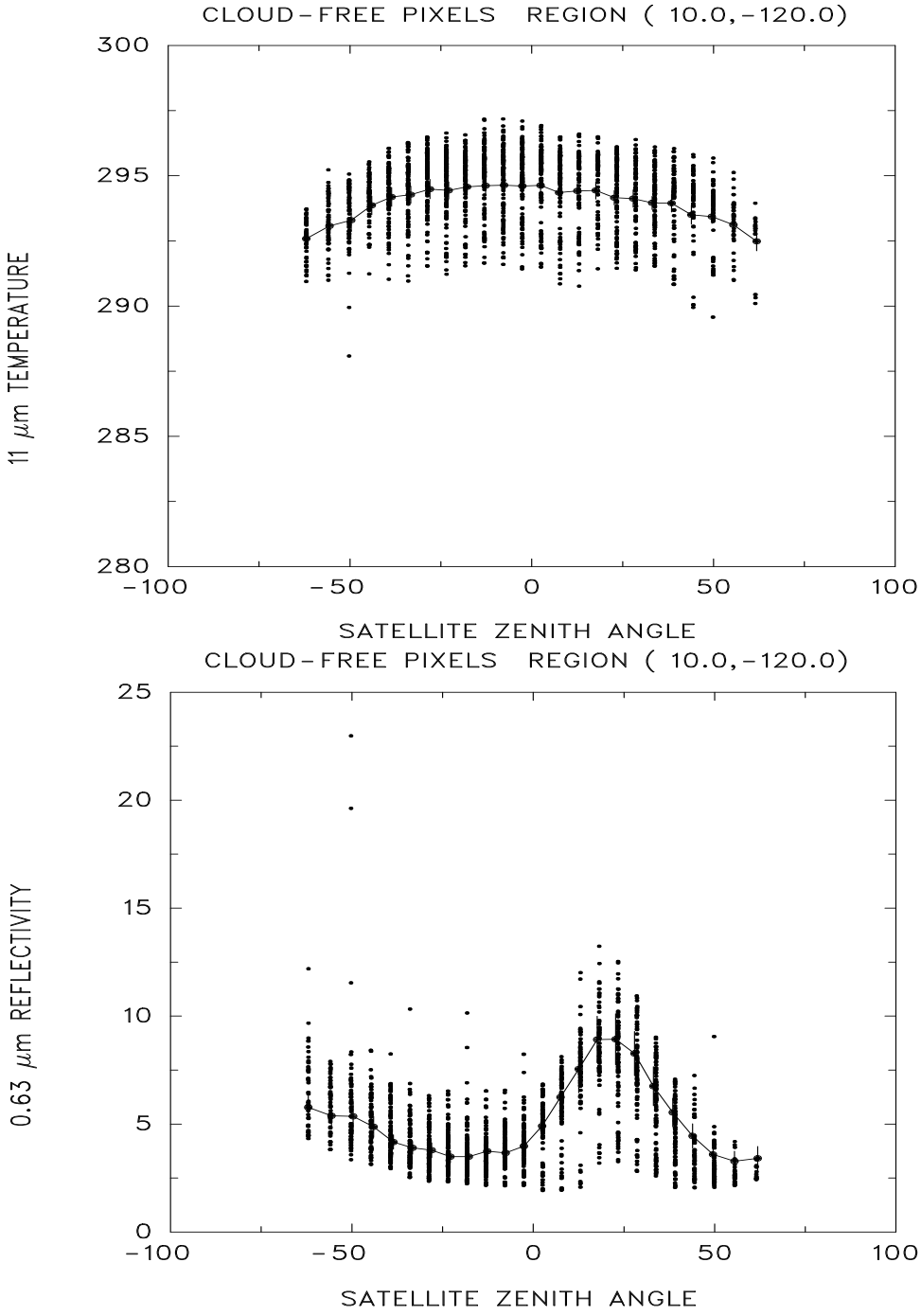

Figure 4.1-5. 11-μm cloud-free radiances (upper frame) and 0.63-μm reflectivities (lower frame) derived from 4-km AVHRR GAC data collected by NOAA-11 for March 1989. The observations are for daytime passes over a 10^o X 10^o latitude-longitude box with 10 N and 120 W being the southwest corner of the box. Each point in the figure gives the average of all cloud-free pixels within a 60-km scale subregion of the 10^o X 10^o latitude-longitude box. The spatial uniformity of reflected and emitted radiances is the only criteria used to identify cloud-free pixels.

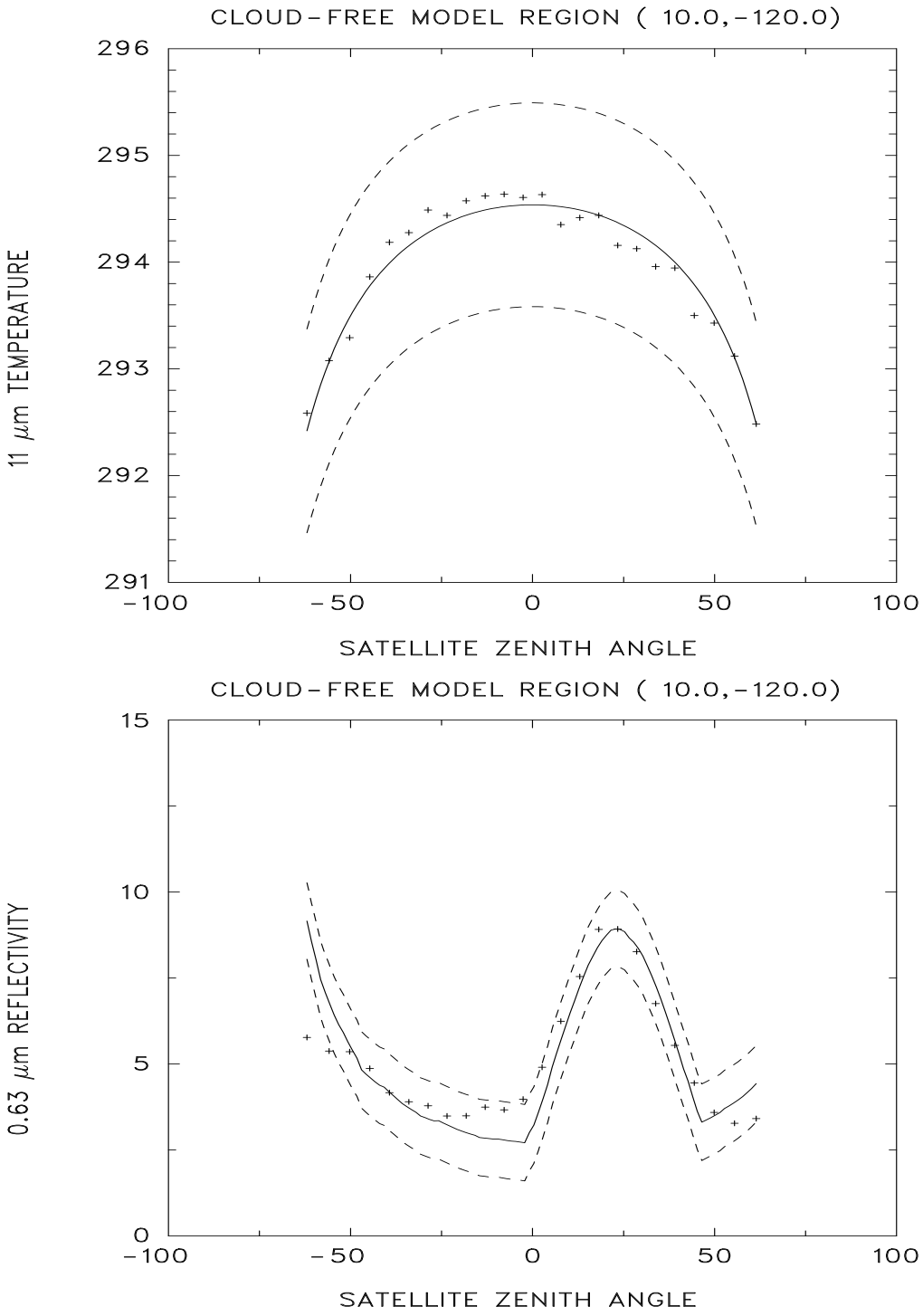

Figure 4.1-6. Means (solid lines) of cloud-free radiances predicted by parametric models for 11-μm radiances (upper frame) and 0.63-μm reflectivities (lower frame) derived from the observations shown in Figure 4.1-5. The dashed curves give one standard deviation of the observed cloud-free radiances on either side of the model predicted means. The crosses give the observed means.

4.1.7. Version 2: Future Directions

4.1.7.1. Detection of Cloud Shadows

The detection of cloud shadows is a problem that has not been addressed adequately in the literature. The following strategy is the first method we will employ to begin determining cloud shadows. The following discussion is only meant to provide an idea of the approach. Further work in this area has been initiated on this problem.

A 3×3 median filter first is applied to reduce noise in the image. It has the following desirable properties: (1) it does not affect the presence or position of the shadow edges, (2) no new brightness values are created, and (3) performance of the Laplace of Gaussian (LOG) zero crossing edge detection algorithm is improved.

4.1.7.1.1. Oceans. Histogram equalization of the AVHRR channel 1 image is made first. The histogram equalization transform produces a histogram that is quasi-uniform on the average. It is based upon the discrete cumulative histogram with quantized brightness values. The dark values on the histogram equalized image are those due to cloud shadows.

4.1.7.1.2. Land. The algorithm over land is more complex because shadows may fall upon both land surfaces of varying reflectances as well as water surfaces such as lakes, rivers, and marshes. The application of a Laplacian filter to a Gaussian filter image is made first. This operation aids in the recognition of shadow and cloud regions. Edge locations are determined by the zero-crossings of the LOG-filtered image. Details are given in Berendes et al. (1992). Many more edges are produced than just cloud and shadow ones. These are due to background variations and to noise.

To isolate the relevant shadow (or cloud) edge pixels, a thresholding procedure is used which is based on a restricted histogram, called the Max/Min histogram. This is constructed from the 3×3 neighborhood surrounding the potential edge pixels. The intention is to capture the modes of the transition pixels generating the edge elements. Generally, there are three distinctive peaks, due to (1) shadows, (2) background, and (3) clouds.

A weighted averaging of the peak values of the Max/Min histogram is used to determine the appropriate threshold between shadow and background (and between cloud and background). This is accomplished by taking into account the size of the distributions. The procedure is iterated to convergence. When water is present in the scene, then a four-mode Max/Min histogram is produced. The same iterative procedure is used to eliminate the background pixels, retaining both shadow and water pixels. The ancillary percent water data set is used to identify probable regions of water.

4.1.7.2. Nighttime Polar Classification

Nighttime polar cloud/surface classification is an extremely difficult problem. Yamanouchi et al. (1987) describe a nighttime polar (Antarctic) cloud/surface discrimination algorithm based upon brightness temperature differences between the AVHRR 3.7- and 10.8-μm channels and between the 10.8- and 12-μm channels. Their cloud/surface discrimination algorithm was more effective over water surfaces than over inland snow-covered surfaces. A number of problems arose over inland snow-covered surfaces. First, the temperature contrast between the cloud and snow surface became especially small, leading to a small brightness temperature difference between the two infrared channels. Second, the AVHRR channels are not well-calibrated at extremely low temperatures (<200 K). As noted in their study, the temperature resolution of channels 4 (10.8-μm) and 5 (12-μm) are approximately 0.6 K at 180 K, while the temperature resolution of channel 3 (3.7-μm) is about 3.5 K at 220 K, and only 7.5 K at 210 K. Therefore, the channel 3 data are not generally useful for cloud detection at the low temperatures expected at the Antarctic. Additionally, the AVHRR data have a digitization problem at extremely low temperatures due to mechanical noise and also because of the nonlinear temperature dependence of

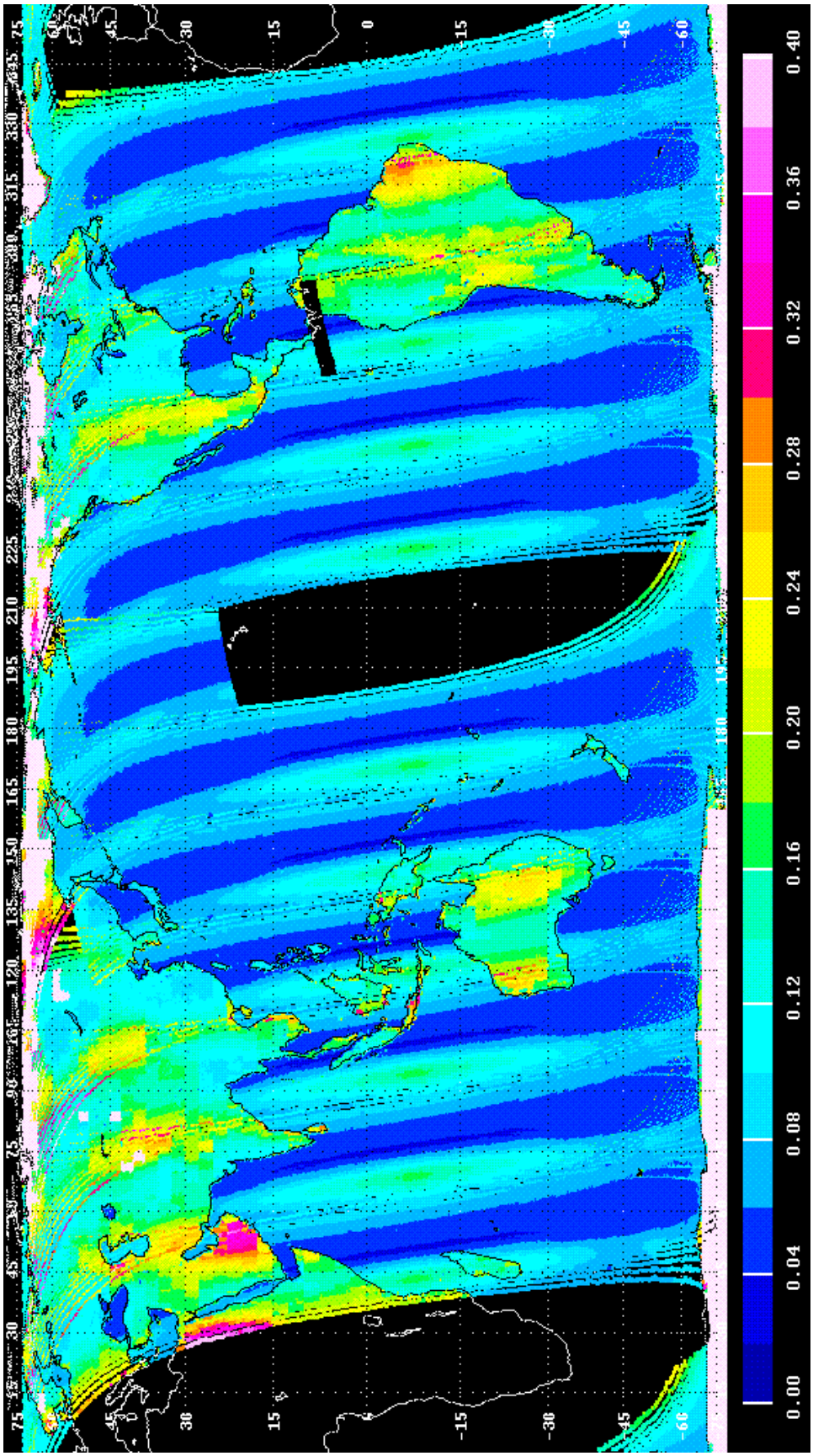

Figure 4.1-7. ISCCP clear-sky reflectance, Oct. 22, 1986.

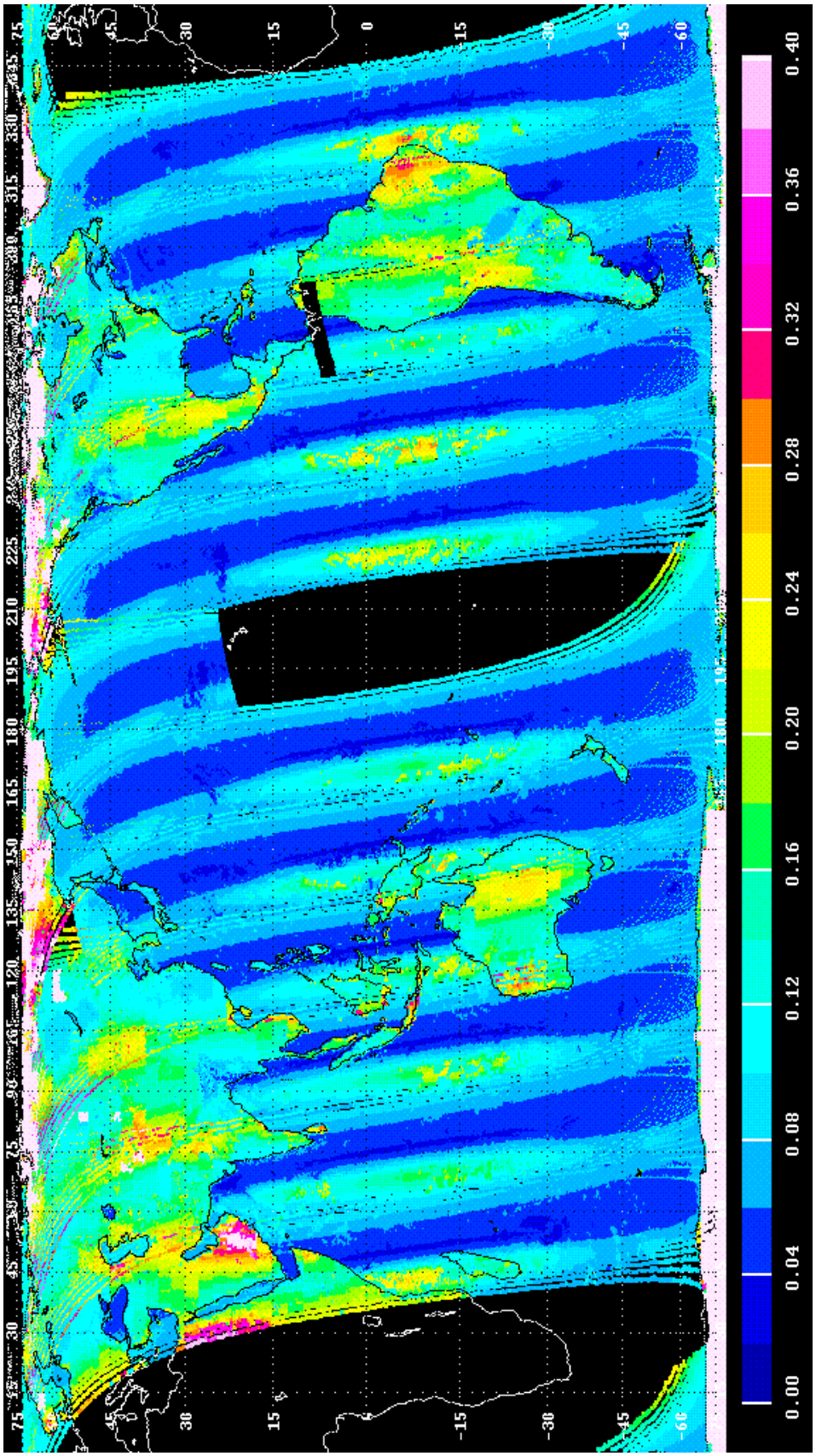

Figure 4.1-8. Revised clear-sky reflectance, Oct. 22, 1986.

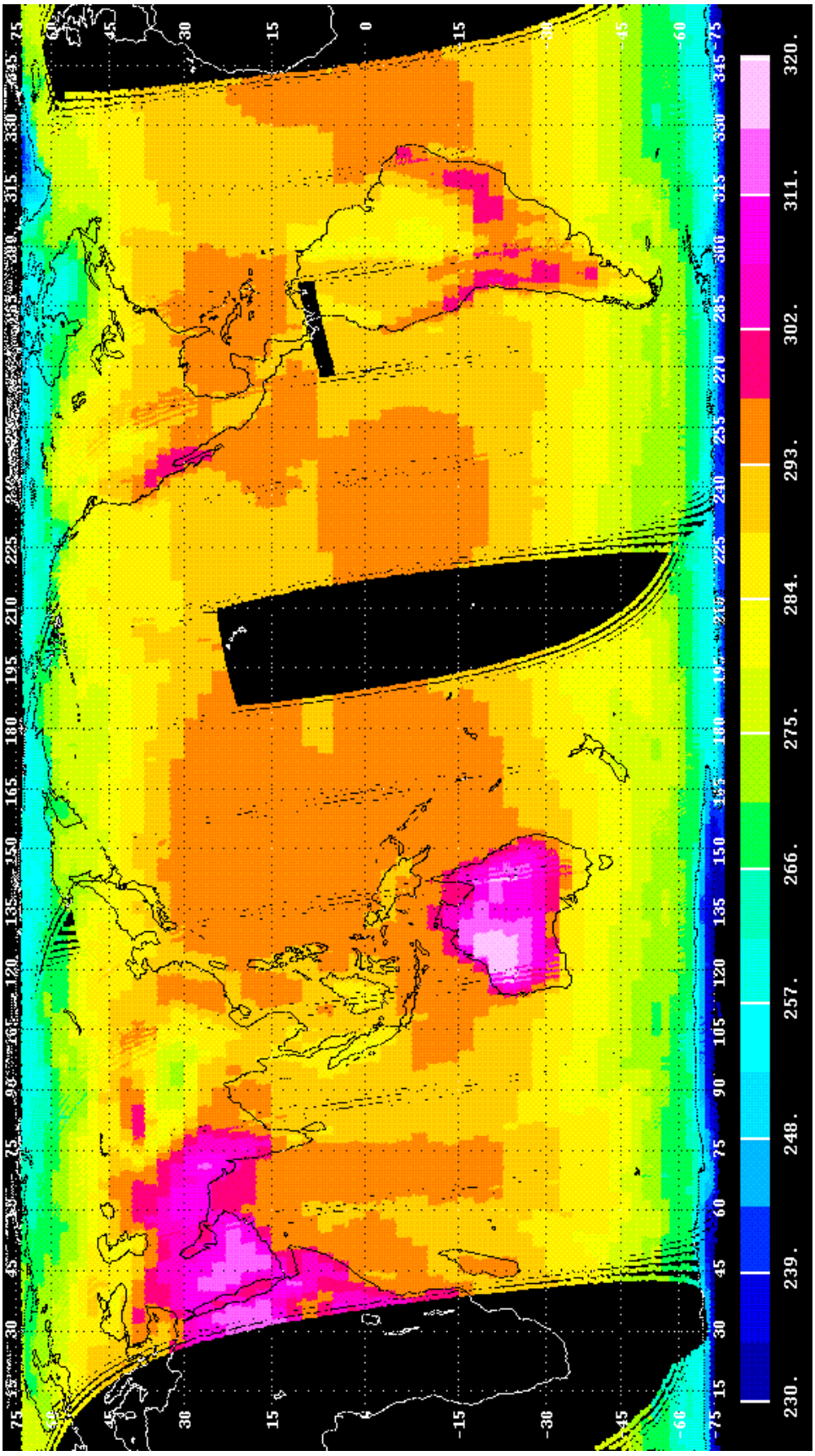

Figure 4.1-9. ISCCP clear-sky temperature (K), Oct. 22, 1986.

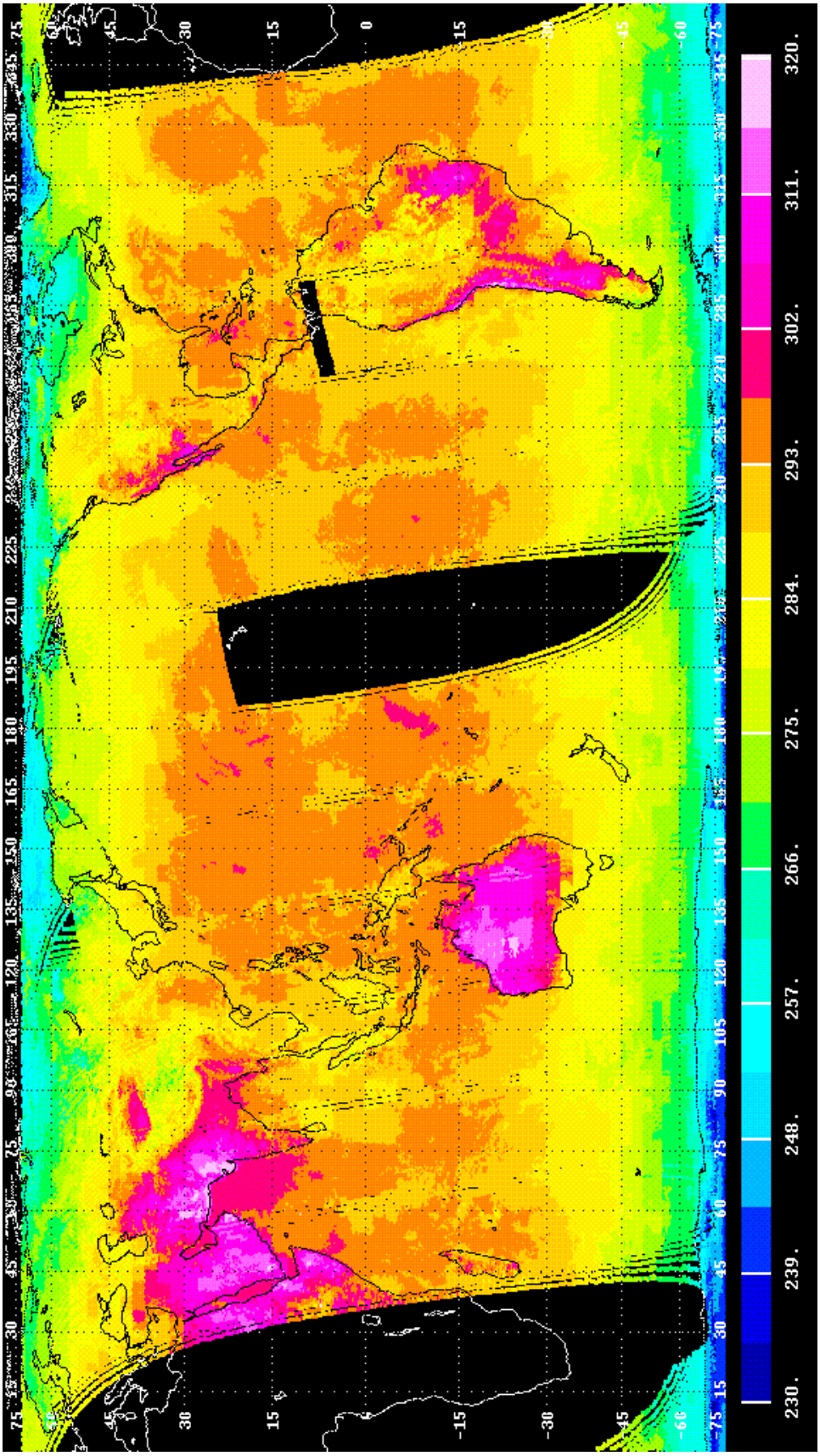

Figure 4.1-10. Revised clear-sky temperature (K), Oct. 22, 1986.

the Planck function. The brightness temperature differences between AVHRR channels 4 and 5 offer the most hope for discriminating clouds from a snow- or ice-covered surface. Much further work needs to be done in this area.

4.1.8. References

Allen, Robert C., Jr.; Durkee, Philip A.; and Wash, Carlyle, H. 1990: Snow/Cloud Discrimination With Multispectral Satellite Measurements. *J. Appl. Meteorol.*, vol. 29, pp. 994–1004.

Berendes, Todd; Sengupta, Sailes K.; Welch, Ron M.; Wielicki, Bruce A.; and Navar, Murgesh 1992: Cumulus Cloud Base Height Estimation From High Spatial Resolution Landsat Data—A Hough Transform Approach. *IEEE Trans. Geosci. & Remote Sens.*, vol. 30, no. 3, pp. 430–443.

Berendes, T., A. Pretre, R. C. Weger, D. Kliche, R. M. Welch, and B. A. Baum, 1996: A paired-histogram approach for automated cloud classification. Submitted to *J. Geophys. Res* for publication.

Brooks, D. R.; Harrison, E. F.; Minnis, P.; Suttles, J. T.; and Kandel, R. S. 1986: Development of Algorithms for Understanding the Temporal and Spatial Variability of the Earth's Radiation Balance. *Rev. Geophys.*, vol. 24, pp. 422–438.

Chen, D. W.; Sengupta, S. K.; and Welch, R. M. 1989: Cloud Field Classification Based upon High Spatial Resolution Textural Features. Part II—Simplified Vector Approaches. *J. Geophys. Res.*, vol. 94, pp. 14749–14765.

Coakley, J. A., Jr.; and Bretherton, F. P. 1982: Cloud Cover from High-Resolution Scanner Data—Detecting and Allowing for Partially Filled Fields of View. *J. Geophys. Res.*, vol. 87, pp. 4917–4932.

Cox, C., and W. Munk, 1954: Statistics of the sea surface derived from sunglitter. *J. Marine Res*., **13**(2), 198-227.

Davis, P.; Stowe, L. L.; and McClain, E. P. 1993: Development of a Cloud Layer Detection Algorithm for the Clouds From AVHRR (CLAVR) Phase II Code. *Proceedings of SPIE Symposium,* SPIE.

Ebert, Elizabeth 1987: A Pattern Recognition Technique for Distinguishing Surface and Cloud Types in the Polar Regions. *J. Climat. & Appl. Meteorol.*, vol. 26, pp. 1412–1427.

Ebert, Elizabeth 1989: Analysis of Polar Clouds From Satellite Imagery Using Pattern Recognition and a Statistical Cloud Analysis Scheme. *J. Appl. Meteorol.*, vol. 28, pp. 382–399.

Foley, J.D. and A. Van Dam, 1984: Fundamentals of Interactive Computer Graphics, Addison-Wesley, ed. 664 pp.

Gao, B-G, and A. F. H. Goetz, 1993: Cirrus cloud detection from airborne imaging spectrometer data using the 1.38-μm water vapor band. *Geophys. Res. Let*., **20**, 301-304.

Garand, Louis 1988: Automated Recognition of Oceanic Cloud Patterns. Part I—Methodology and Application to Cloud Climatology. *J. Climat.*, vol. 1, pp. 20–39.

Giarratano, Joseph C.; and Riley, Gary 1989: *Expert Systems: Principles and Programming*. PWS-Kent Publ. Co.

Gutman, G.; Tarpley, D.; and Ohring, G. 1987: Cloud Screening for Determination of Land Surface Characteristics in a Reduced Resolution Satellite Data Set. *Int. J. Remote Sens.*, vol. 8, pp. 859–870.

Haralick, R. M.; Dinstein, I.; and Shanmugam, K. 1973: Textural Features for Image Classification. *IEEE Trans. Syst., Man, & Cybern.*, vol. SMC-3, pp. 610–621.

Hecht-Nielsen, Robert 1990: *Neurocomputing*. Addison-Wesley Publ. Co.

Inoue, Toshiro 1987: A Cloud Type Classification with NOAA 7 Split-Window Measurements. *J. Geophys. Res.*, vol. 92, pp. 3991–4000.

Inoue, Toshiro 1989: Features of Clouds Over the Tropical Pacific During Northern Hemispheric Winter Derived From Split Window Measurements. *J. Meteorol. Soc. Japan*, vol. 67, pp. 621–637.

Key, J.; and Barry R. G. 1989: Cloud Cover Analysis With Arctic AVHRR Data. I—Cloud Detection. *J. Geophys. Res.*, vol. 94, pp. 18521–18535.

Kidwell, K. B., 1991: NOAA Polar Orbiter User's Guide, NOAA Climate Data Center, Satellite Data Services Division, Washington, D. C.

Kriebel, K. T. 1978: Measured Spectral Bidirectional Reflection Properties of Four Vegetated Surfaces. *Appl. Opt.*, vol. 17, pp. 253–259.

Lee, Jonathan; Weger, Ronald C.; Sengupta, Sailes K.; and Welch, Ronald M. 1990: A Neural Network Approach to Cloud Classification. *IEEE Trans. Geosci. & Remote Sens.*, vol. 28, pp. 846–855.

Levine, J. S., W. R. Cofer III, D. R. Cahoon, Jr., and E. L. Winstead, 1995: Biomass burning: A driver for global change. *Environmental Science and Technology*, **29**, 120-125.

Luger, George F.; and Stubblefield, William A. 1989: *Artificial Intelligence and the Design of Expert Systems*. Benjamin/Cummings Publ. Co.

Matthews, Elaine; and Rossow William B. 1987: Regional and Seasonal Variations of Surface Reflectance From Satellite Observations at 0.6 micron. *J. Climat. & Appl. Meteorol.*, vol. 26, pp. 170–202.

McClain, E. P. 1993: *Evaluation of CLAVR Phase-I Algorithm Performance—Final Report*. U.S. Department of Commerce/ NOAA/NESDIS, Report 40-AANE-201-424.

Minnis, P.; and Harrison, E. F. 1984a: Diurnal Variability of Regional Cloud and Clear-Sky Radiative Parameters Derived From GOES Data. Part I—Analysis Method. *J. Climat. & Appl. Meteorol.*, vol. 23, pp. 993–1011.

Minnis, P.; and Harrison, E. F. 1984b: Diurnal Variability of Regional Cloud and Clear-Sky Radiative Parameters Derived from GOES Data. Part II—November 1978 Cloud Distributions. *J. Climat. & Appl. Meteorol.*, vol. 23, pp. 1012–1031.

Minnis, P.; and Harrison, E. F. 1984c: Diurnal Variability of Regional Cloud and Clear-Sky Radiative Parameters Derived From GOES Data. Part III—November 1978 Radiative Parameters. *J. Climat. & Appl. Meteorol.*, vol. 23, pp. 1032–1051.

Minnis, Patrick; Harrison, Edwin F.; and Gibson, Gary G. 1987: Cloud Cover Over the Equatorial Eastern Pacific Derived From July 1983 International Satellite Cloud Climatology Project Data Using a Hybrid Bispectral Threshold Method. *J. Geophys. Res.*, vol. 92, pp. 4051–4073.

Richards, J. A., Remote Sensing Digital Image Analysis. 2nd Edition, Springer-Verlag, New York. 340 pp., 1993.

Rossow, William B. 1989: Measuring Cloud Properties From Space—A Review. *J. Climat.*, vol. 2, pp. 201–213.

Rossow, William B.; and Garder, Leonid C. 1993: Cloud Detection Using Satellite Measurements of Infrared and Visible Radiances for ISCCP. *J. Climat.*, vol. 6, no. 12, pp. 2341–2369.

Rumelhart, D. E.; Hinton, G.; and Williams, R. 1986: Learning Internal Representations by Error Propagation. In *Parallel Distribution Distributed Processing—Exploration in the Microstructure of Cognition*. D. Rumelhart and J. McClelland, eds., MIT Press, pp. 318–362.

Saunders, R. W.; and Kriebel K. T. 1988: An Improved Method for Detecting Clear Sky and Cloudy Radiances From AVHRR Data. *Int. J. Remote Sens.*, vol. 9, pp. 123–150.

Seze, Genevieve; and Desbois, Michel 1987: Cloud Cover Analysis From Satellite Imagery Using Spatial and Temporal Characteristics of the Data. *J. Climat. & Appl. Meteorol.*, vol. 26, pp. 287–303.

Seze, Genevieve; Rossow, William B. 1991a: Time-Cumulated Visible and Infrared Radiance Histograms Used as Descriptors of Surface and Cloud Variations. *Int. J. Remote Sens.*, vol. 12, pp. 877–920.

Seze, Genevieve; and Rossow, William B. 1991b: Effects of Satellite Data Resolution on Measuring the Space/Time Variations of Surfaces and Clouds. *Int. J. Remote Sens.*, vol. 12, pp. 921–952.

Stowe, L. L.; McClain, E. P.; Carey, R.; Pellegrino, P.; and Gutman, G. G. 1991: Global Distribution of Cloud Cover Derived From NOAA/AVHRR Operational Satellite Data. *Adv. Space Res.*, vol. 11, no. 3, pp. 51–54.

Stowe, L. L.; Vemury, S. K.; and Rao, A. V. 1994: AVHRR Clear Sky Radiation Data Sets at NOAA/NESDIS. *Adv. Space Res.*, vol. 11, pp. 113–116.

Suttles, J. T.; Green, R. N.; Minnis, P.; Smith, G. L.; Staylor, W. F.; Wielicki, B. A.; Walker, I. J.; Young, D. F.; Taylor, V. R.; and Stowe, L. L. 1988: *Angular Radiation Models for Earth-Atmosphere System. Volume I: Shortwave Radiation.* NASA RP-1184.

Tarpley, J. D. 1979: Estimating Incident Solar Radiation at the Surface From Geostationary Satellite Data. *J. Appl. Meteorol.* vol. 18, pp. 1172–1181.

Tovinkere, V. R.; Penaloza, M.; Logar, A.; Lee, J.; Weger, R. C.; Berendes, T. A.; and Welch, R. M. 1993: An Intercomparison of Artificial Intelligence Approaches for Polar Scene Identification. *J. Geophys. Res.*, vol. 98, no. D3, pp. 5001–5016.

Welch, R. M.; Sengupta, S. K.; Goroch, A. K.; Rabindra, P.; Rangaraj, N.; and Navar, M. S. 1992: Polar Cloud and Surface Classification Using AVHRR Imagery—An Intercomparison of Methods. *J. Appl. Meteorol.*, vol. 31, no. 5, pp. 405–420.

Welch, Ronald M.; Kuo, Kwo-Sen; and Sengupta, Sailes K. 1990: Cloud and Surface Textural Features in Polar Regions. *IEEE Trans. Geosci. & Remote Sens.*, vol. 28, pp. 520–528.

Welch, R. M.; Navar, M. S.; and Sengupta, S. K. 1989: The Effect of Spatial Resolution Upon Texture-Based Cloud Field Classifications. *J. Geophys. Res.*, vol. 94, pp. 14767–14781.

Yamanouchi, Takashi; Kawaguchi, Sadao; and Suzuki, Kazuya 1987: Detection of Clouds in Antarctica From Infrared Multispectral Data of AVHRR. *J. Meteorol. Soc. Japan*, vol. 65, pp. 949–962.

Appendix A

Nomenclature

Acronyms

ADEOS	Advanced Earth Observing System
ADM	Angular Distribution Model
AIRS	Atmospheric Infrared Sounder (EOS-AM)
AMSU	Advanced Microwave Sounding Unit (EOS-PM)
APD	Aerosol Profile Data
APID	Application Identifier
ARESE	ARM Enhanced Shortwave Experiment
ARM	Atmospheric Radiation Measurement
ASOS	Automated Surface Observing Sites
ASTER	Advanced Spaceborne Thermal Emission and Reflection Radiometer
ASTEX	Atlantic Stratocumulus Transition Experiment
ASTR	Atmospheric Structures
ATBD	Algorithm Theoretical Basis Document
AVG	Monthly Regional, Average Radiative Fluxes and Clouds (CERES Archival Data Product)
AVHRR	Advanced Very High Resolution Radiometer
BDS	Bidirectional Scan (CERES Archival Data Product)
BRIE	Best Regional Integral Estimate
BSRN	Baseline Surface Radiation Network
BTD	Brightness Temperature Difference(s)
CCD	Charge Coupled Device
CCSDS	Consultative Committee for Space Data Systems
CEPEX	Central Equatorial Pacific Experiment
CERES	Clouds and the Earth's Radiant Energy System
CID	Cloud Imager Data
CLAVR	Clouds from AVHRR
CLS	Constrained Least Squares
COPRS	Cloud Optical Property Retrieval System
CPR	Cloud Profiling Radar
CRH	Clear Reflectance, Temperature History (CERES Archival Data Product)
CRS	Single Satellite CERES Footprint, Radiative Fluxes and Clouds (CERES Archival Data Product)
DAAC	Distributed Active Archive Center
DAC	Digital-Analog Converter
DAO	Data Assimilation Office

DB	Database
DFD	Data Flow Diagram
DLF	Downward Longwave Flux
DMSP	Defense Meteorological Satellite Program
EADM	ERBE-Like Albedo Directional Model (CERES Input Data Product)
ECA	Earth Central Angle
ECLIPS	Experimental Cloud Lidar Pilot Study
ECMWF	European Centre for Medium-Range Weather Forecasts
EDDB	ERBE-Like Daily Data Base (CERES Archival Data Product)
EID9	ERBE-Like Internal Data Product 9 (CERES Internal Data Product)
EOS	Earth Observing System
EOSDIS	Earth Observing System Data Information System
EOS-AM	EOS Morning Crossing Mission
EOS-PM	EOS Afternoon Crossing Mission
ENSO	El Niño/Southern Oscillation
ENVISAT	Environmental Satellite
EPHANC	Ephemeris and Ancillary (CERES Input Data Product)
ERB	Earth Radiation Budget
ERBE	Earth Radiation Budget Experiment
ERBS	Earth Radiation Budget Satellite
ESA	European Space Agency
ES4	ERBE-Like S4 Data Product (CERES Archival Data Product)
ES4G	ERBE-Like S4G Data Product (CERES Archival Data Product)
ES8	ERBE-Like S8 Data Product (CERES Archival Data Product)
ES9	ERBE-Like S9 Data Product (CERES Archival Data Product)
FLOP	Floating Point Operation
FIRE	First ISCCP Regional Experiment
FIRE II IFO	First ISCCP Regional Experiment II Intensive Field Observations
FOV	Field of View
FSW	Hourly Gridded Single Satellite Fluxes and Clouds (CERES Archival Data Product)
FTM	Functional Test Model
GAC	Global Area Coverage (AVHRR data mode)
GAP	Gridded Atmospheric Product (CERES Input Data Product)
GCIP	GEWEX Continental-Phase International Project
GCM	General Circulation Model
GEBA	Global Energy Balance Archive
GEO	ISSCP Radiances (CERES Input Data Product)
GEWEX	Global Energy and Water Cycle Experiment
GLAS	Geoscience Laser Altimetry System

GMS	Geostationary Meteorological Satellite
GOES	Geostationary Operational Environmental Satellite
HBTM	Hybrid Bispectral Threshold Method
HIRS	High-Resolution Infrared Radiation Sounder
HIS	High-Resolution Interferometer Sounder
ICM	Internal Calibration Module
ICRCCM	Intercomparison of Radiation Codes in Climate Models
ID	Identification
IEEE	Institute of Electrical and Electronics Engineers
IES	Instrument Earth Scans (CERES Internal Data Product)
IFO	Intensive Field Observation
INSAT	Indian Satellite
IOP	Intensive Observing Period
IR	Infrared
IRIS	Infrared Interferometer Spectrometer
ISCCP	International Satellite Cloud Climatology Project
ISS	Integrated Sounding System
IWP	Ice Water Path
LAC	Local Area Coverage (AVHRR data mode)
LaRC	Langley Research Center
LBC	Laser Beam Ceilometer
LBTM	Layer Bispectral Threshold Method
Lidar	Light Detection and Ranging
LITE	Lidar In-Space Technology Experiment
Lowtran 7	Low-Resolution Transmittance (Radiative Transfer Code)
LW	Longwave
LWP	Liquid Water Path
MAM	Mirror Attenuator Mosaic
MC	Mostly Cloudy
MCR	Microwave Cloud Radiometer
METEOSAT	Meteorological Operational Satellite (European)
METSAT	Meteorological Satellite
MFLOP	Million FLOP
MIMR	Multifrequency Imaging Microwave Radiometer
MISR	Multiangle Imaging Spectroradiometer
MLE	Maximum Likelihood Estimate
MOA	Meteorology Ozone and Aerosol
MODIS	Moderate-Resolution Imaging Spectroradiometer
MSMR	Multispectral, multiresolution

MTSA	Monthly Time and Space Averaging
MWH	Microwave Humidity
MWP	Microwave Water Path
NASA	National Aeronautics and Space Administration
NCAR	National Center for Atmospheric Research
NCEP	National Centers for Environmental Prediction
NESDIS	National Environmental Satellite, Data, and Information Service
NIR	Near Infrared
NMC	National Meteorological Center
NOAA	National Oceanic and Atmospheric Administration
NWP	Numerical Weather Prediction
OLR	Outgoing Longwave Radiation
OPD	Ozone Profile Data (CERES Input Data Product)
OV	Overcast
PC	Partly Cloudy
POLDER	Polarization of Directionality of Earth's Reflectances
PRT	Platinum Resistance Thermometer
PSF	Point Spread Function
PW	Precipitable Water
RAPS	Rotating Azimuth Plane Scan
RPM	Radiance Pairs Method
RTM	Radiometer Test Model
SAB	Sorting by Angular Bins
SAGE	Stratospheric Aerosol and Gas Experiment
SARB	Surface and Atmospheric Radiation Budget Working Group
SDCD	Solar Distance Correction and Declination
SFC	Hourly Gridded Single Satellite TOA and Surface Fluxes (CERES Archival Data Product)
SHEBA	Surface Heat Budget in the Arctic
SPECTRE	Spectral Radiance Experiment
SRB	Surface Radiation Budget
SRBAVG	Surface Radiation Budget Average (CERES Archival Data Product)
SSF	Single Satellite CERES Footprint TOA and Surface Fluxes, Clouds
SSMI	Special Sensor Microwave Imager
SST	Sea Surface Temperature
SURFMAP	Surface Properties and Maps (CERES Input Product)
SW	Shortwave
SWICS	Shortwave Internal Calibration Source
SYN	Synoptic Radiative Fluxes and Clouds (CERES Archival Data Product)

SZA	Solar Zenith Angle
THIR	Temperature/Humidity Infrared Radiometer (Nimbus)
TIROS	Television Infrared Observation Satellite
TISA	Time Interpolation and Spatial Averaging Working Group
TMI	TRMM Microwave Imager
TOA	Top of the Atmosphere
TOGA	Tropical Ocean Global Atmosphere
TOMS	Total Ozone Mapping Spectrometer
TOVS	TIROS Operational Vertical Sounder
TRMM	Tropical Rainfall Measuring Mission
TSA	Time-Space Averaging
UAV	Unmanned Aerospace Vehicle
UT	Universal Time
UTC	Universal Time Code
VAS	VISSR Atmospheric Sounder (GOES)
VIRS	Visible Infrared Scanner
VISSR	Visible and Infrared Spin Scan Radiometer
WCRP	World Climate Research Program
WG	Working Group
Win	Window
WN	Window
WMO	World Meteorological Organization
ZAVG	Monthly Zonal and Global Average Radiative Fluxes and Clouds (CERES Archival Data Product)

Symbols

A	atmospheric absorptance
$B_\lambda(T)$	Planck function
C	cloud fractional area coverage
CF_2Cl_2	dichlorofluorocarbon
$CFCl_3$	trichlorofluorocarbon
CH_4	methane
CO_2	carbon dioxide
D	total number of days in the month
D_e	cloud particle equivalent diameter (for ice clouds)
E_o	solar constant or solar irradiance
F	flux
f	fraction
G_a	atmospheric greenhouse effect

g	cloud asymmetry parameter
H_2O	water vapor
I	radiance
i	scene type
m_i	imaginary refractive index
$\hat{N}$	angular momentum vector
N_2O	nitrous oxide
O_3	ozone
P	point spread function
p	pressure
Q_a	absorption efficiency
Q_e	extinction efficiency
Q_s	scattering efficiency
R	anisotropic reflectance factor
r_E	radius of the Earth
r_e	effective cloud droplet radius (for water clouds)
r_h	column-averaged relative humidity
S_o	summed solar incident SW flux
S_o'	integrated solar incident SW flux
T	temperature
T_B	blackbody temperature
t	time or transmittance
W_{liq}	liquid water path
w	precipitable water
$\hat{x}_o$	satellite position at t_o
x, y, z	satellite position vector components
$\dot{x}, \dot{y}, \dot{z}$	satellite velocity vector components
z	altitude
z_{top}	altitude at top of atmosphere
α	albedo or cone angle
β	cross-scan angle
γ	Earth central angle
γ_{at}	along-track angle
γ_{ct}	cross-track angle
δ	along-scan angle
ε	emittance
Θ	colatitude of satellite
θ	viewing zenith angle
θ_o	solar zenith angle

λ	wavelength
μ	viewing zenith angle cosine
μ_o	solar zenith angle cosine
ν	wave number
ρ	bidirectional reflectance
τ	optical depth
$\tau_{aer}(p)$	spectral optical depth profiles of aerosols
$\tau_{H_2O\lambda}(p)$	spectral optical depth profiles of water vapor
$\tau_{O_3}(p)$	spectral optical depth profiles of ozone
Φ	longitude of satellite
ϕ	azimuth angle
$\tilde{\omega}_o$	single-scattering albedo

Subscripts:

c	cloud
cb	cloud base
ce	cloud effective
cld	cloud
cs	clear sky
ct	cloud top
ice	ice water
lc	lower cloud
liq	liquid water
s	surface
uc	upper cloud
λ	spectral wavelength

Units

AU	astronomical unit
cm	centimeter
cm-sec^{-1}	centimeter per second
count	count
day	day, Julian date
deg	degree
deg-sec^{-1}	degree per second
DU	Dobson unit
erg-sec^{-1}	erg per second
fraction	fraction (range of 0–1)
g	gram
g-cm^{-2}	gram per square centimeter

$g\text{-}g^{-1}$	gram per gram
$g\text{-}m^{-2}$	gram per square meter
h	hour
hPa	hectopascal
K	Kelvin
kg	kilogram
$kg\text{-}m^{-2}$	kilogram per square meter
km	kilometer
$km\text{-}sec^{-1}$	kilometer per second
m	meter
mm	millimeter
μm	micrometer, micron
N/A	not applicable, none, unitless, dimensionless
$ohm\text{-}cm^{-1}$	ohm per centimeter
percent	percent (range of 0–100)
rad	radian
$rad\text{-}sec^{-1}$	radian per second
sec	second
sr^{-1}	per steradian
W	watt
$W\text{-}m^{-2}$	watt per square meter
$W\text{-}m^{-2}sr^{-1}$	watt per square meter per steradian
$W\text{-}m^{-2}sr^{-1}\mu m^{-1}$	watt per square meter per steradian per micrometer